Investigation of structural and magnetic properties of NiO/BaFe$_{12}$O$_{19}$/Ni$_{0.5}$Zn$_{0.5}$Fe$_2$O$_4$ nanocomposites

S. Farhat[1] · R. Awad[2,3] · Z. Bitar[1]

Abstract

Pure NiO, BaFe$_{12}$O$_{19}$, and Ni$_{0.5}$Zn$_{0.5}$Fe$_2$O$_4$ nanoparticles were synthesized by the co-precipitation method. Four ternary $(1-x-y)$NiO/xNi$_{0.5}$Zn$_{0.5}$Fe$_2$O$_4$/yBaFe$_{12}$O$_{19}$ (x and y between 0 and 1) nanocomposites (NCs) were prepared by the wet ball milling technique, then calcined at 950 °C for 4 h. The X-ray powder diffraction (XRD) validated the production of pure NiO and Ni$_{0.5}$Zn$_{0.5}$Fe$_2$O$_4$ without impurities, while BaFe$_{12}$O$_{19}$ was produced with the α-Fe$_2$O$_3$ additional phase. When compared to the initial weight percentages, the Rietveld refinement technique revealed different weight percentages for the three phases. The transmission electron microscope (TEM) and the selected area electron diffraction (SAED) investigated the morphology and the microstructure of the samples, respectively. X-ray photoelectron spectroscopy (XPS) showed that nanocomposites were successfully formed from the examination of the elements constituting the nanocomposites (Ba^{2+}, Ni^{2+}, Ni^{3+}, Zn^{2+}, Fe^{3+}and O^{2-}). The vibrating sample magnetometer (VSM) measurements identified the effect of the weight percentage of each phase in the nanocomposite on the magnetic parameters. The switching field distribution (SFD) curves indicated significant exchange coupling interactions in the samples that include a small weight percentage of BaFe$_{12}$O$_{19}$. Exchange and dipolar interactions were both recognized in Henkel plots of all samples, although exchange coupling predominated. Four laws of approach to saturation (LAS) were applied to the samples and showed magnetization dependency on H^{-1} and H$^{-1/2}$ rather than the summation of H^{-1}, H^{-2}, and H for almost all samples.

Keywords NiO/BaFe$_{12}$O$_{19}$/Ni$_{0.5}$Zn$_{0.5}$Fe$_2$O$_4$ · Nanocomposites · VSM · XPS · Exchange coupling

1 Introduction

Numerous investigations have been conducted on nanocomposite magnetic materials because the combination of several magnets at the nanoscale can significantly enhance the overall magnetic properties [1]. Magnetic nanocomposites can be employed widely in energy storage applications [2], magnetic recording media [3, 4], microwave devices [5], permanent magnets [6], and biomedicines [7]. Theoretically, an exchange-coupled nanocomposite with saturation magnetization and

energy products that are larger than those of single magnetic-phase magnets is obtained by combining a hard magnetic phase with its high coercive field with a soft magnetic phase with its high saturation magnetization, as it was proposed by Kneller et al. [8]. Several investigations on these hard/soft exchange-coupled materials systems have been conducted recently [9, 10]. The magnetic behavior of BaFe$_{12}$O$_{19}$ + (x) CuFe$_2$O$_4$ (with x = 1, 2, and 4) produced by the conventional sol–gel method was explored by Manglam et al. [11]. They discovered that the composite BaFe$_{12}$O$_{19}$ + CuFe$_2$O$_4$ (i.e., x = 1) has the highest magnetic characteristics (saturation magnetization (M$_s$), Coercivity (H$_c$), and the maximum energy product (BH)$_{max}$) among all the composite samples studied. This composite (BaFe$_{12}$O$_{19}$ + CuFe$_2$O$_4$) was annealed at various temperatures to optimize its magnetic properties. They found that the annealing temperature (1000 °C) yields the maximum energy product (BH)$_{max}$ and saturation magnetization (M$_s$). Almessiere et al. [12] prepared hard/soft (H/S) Sr$_{0.5}$Ba$_{0.5}$Eu$_{0.01}$Fe$_{12}$O$_{19}$/Ni$_x$Cu$_y$Zn$_w$Fe$_2$O$_4$ nanocomposites (NCs) via a one-pot sol–gel auto-combustion method. They

✉ Z. Bitar
zouheirbitar@hotmail.com

1   Physics Department, Faculty of Science, Beirut Arab University, Beirut, Lebanon

2   Physics Department, Faculty of Science, Alexandria University, Alexandria, Egypt

3   Department of Basic Sciences, Faculty of Computer Science and Artificial Intelligence, Pharos University in Alexandria, Alexandria, Egypt

studied the effects of varying the Ni, Cu, and Zn ratios on the structural, magnetic, and microwave (MW) properties of these NCs. It was found that the electrodynamic characteristics were significantly influenced by the stoichiometry of the Ni, Cu, and Zn ions in the spinel fraction. The prepared samples could be good candidates for use in radar-based systems because of their small reflectivity. $Ni_{0.5}Zn_{0.5}Fe_2O_4$ is a soft spinel ferrite with high saturation magnetization and Curie temperature, good mechanical hardness, strong chemical stability [13], and low coercivity. This ferrite is a great core material for power transformers in electronic and telecommunication applications due to its high electrical resistance and good magnetic characteristics [14]. Additionally, M-type hexaferrite, specifically barium hexaferrite ($BaFe_{12}O_{19}$), has been playing a dominant role in science and commerce as one of the most significant permanent magnetic materials due to a special combination of beneficial properties like their high intrinsic coercivity (H_c), high chemical stability, large crystalline anisotropy, low production cost [15], moderate saturation magnetization, high Curie temperature, and notable corrosion resistance [16]. Many researchers have worked on the soft/hard ferrites nanocomposites consisting of $Ni_{0.5}Zn_{0.5}Fe_2O_4$ and $BaFe_{12}O_{19}$ to combine the properties of both phases and to make exchange-coupled nanocomposites [17–19]. Nikmanesh et al. [20] synthesized $BaFe_{12}O_{19}/Ni_{0.6}Zn_{0.4}Fe_2O_4$ nanocomposites with different weight percentages by a physical mixing method at various annealing temperatures (T = 700 °C to 900 °C). They demonstrated the coexistence of the soft and hard phases with uniform distribution in the nanocomposites. Additionally, they concluded that the molar ratio of hard to soft phase and the sintering temperature significantly affected magnetic characteristics of the nanocomposites. They proved good exchange coupling in samples annealed at temperature above 800 °C while the hard and soft phases in the NCs annealed at 700 °C are weakly exchange coupled. Moreover, nickel oxide is a typical p-type metal oxide semiconductor with a large energy gap of 3.6–4 eV. It exhibits a large specific surface area, excellent structural stability, significant transport abilities, and a high capability for oxygen adsorption [21]. It has numerous applications as supercapacitors [22], anodes for lithium-ion batteries [23], and photocatalysts in dye wastewater treatment [24]. NiO thin films have also been used in dye-sensitized solar cells [25], gas sensors [26], and optoelectronic devices [27]. Several studies investigated the combination of NiO with other metal oxides and ferrites to form binary and ternary nanocomposites with new properties and multiple functionalities. Gong et al. [28] investigated the exchange bias (EB) effect in $(100 - x)NiO/(x)NiFe_2O_4$ nanocomposites synthesized by a chemical co-precipitation method. They found that the presence of ferrimagnetic $NiFe_2O_4$ nanoparticles is what causes the greatest EB field H_E of the nanocomposites with x = 2.5. Yassine et al. [29] studied the effects of varying the amount of NiO and $CdFe_2O_4$ in $(x)NiO/(1 - x)CdFe_2O_4$

nanocomposites for x = 0, 0.1, 0.2, 0.3, 0.4, 0.5 and 1 on the structural, optical and magnetic properties. They concluded that the produced nanocomposites can be viable candidates for use as soft magnets due to their low coercivities and moderate saturation magnetizations. Munawar et al. [30] synthesized NiO–CdO–ZnO mixed ternary oxide nanocomposites by the homogeneous co-precipitation method. They investigated their structural, optical, and electrical properties, and photocatalytic activity. They found that the multimetal oxide NiO–CdO–ZnO was an effective candidate for usage as a sunlight-driven photocatalyst. This work expects that the remarkable properties of NiO, $Ni_{0.5}Zn_{0.5}Fe_2O_4$, and $BaFe_{12}O_{19}$ would give good results when they are joined together in nanocomposites. The three constituent components of the nanocomposites are expected to exhibit synergistic interactions resulting in new materials with improved and distinctive properties. To the authors' knowledge, no prior work has mixed these three components with the given concentrations in ternary nanocomposites and investigated the magnetic effect of each phase on the other. Consequently, the results presented here can make an important contribution to the research field of oxide/hard/soft ferrite nanocomposites. In this work, pure NiO, $BaFe_{12}O_{19}$, and $Ni_{0.5}Zn_{0.5}Fe_2O_4$ were synthesized by the wet-chemical co-precipitation method. Four ternary oxide/hard/soft ferrite nanocomposites: C1 ($0.33NiO$, $0.33BaFe_{12}O_{19}$, $0.33Ni_{0.5}Zn_{0.5}Fe_2O_4$), C2 ($0.66NiO$, $0.166BaFe_{12}O_{19}$, $0.166Ni_{0.5}Zn_{0.5}Fe_2O_4$), C3 ($0.166NiO$, $0.66BaFe_{12}O_{19}$, $0.166Ni_{0.5}Zn_{0.5}Fe_2O_4$), and C4 ($0.166NiO$, $0.166BaFe_{12}O_{19}$, $0.66Ni_{0.5}Zn_{0.5}Fe_2O_4$) were prepared by wet ball-milling technique and then calcined at 950 °C for 4 h. The structural, morphological, and magnetic properties of the three pure nano samples and four nanocomposites were thoroughly investigated in this work. This study highlights a remarkable gap in the existing literature by focusing on ternary nanocomposites, a part that has been given less attention compared to binary nanocomposites. The importance of this work is bifold: first, we investigated the interface interactions within four ternary systems, revealing distinct behaviors dependent on the weight percentages of each phase. Second, by synthesizing four ternary nanocomposites using the same method and under similar conditions, the reproducibility, reliability and comparability of the findings in this work were enhanced.

2 Methods and materials

2.1 Preparation of $Ni_{0.5}Zn_{0.5}Fe_2O_4$, $BaFe_{12}O_{19}$, and NiO nanoparticles

All pure nanoparticles $Ni_{0.5}Zn_{0.5}Fe_2O_4$, $BaFe_{12}O_{19}$, and NiO were prepared using the wet chemical co-precipitation method. To prepare a $Ni_{0.5}Zn_{0.5}Fe_2O_4$ solution, so-called

solution 1, 1 M of each of the raw materials from Sigma Aldrich: Iron (III) chloride hexahydrate ($FeCl_3.6H_2O$), Nickel (II) chloride hexahydrate ($NiCl_2.6H_2O$), and Zinc chloride ($ZnCl_2$) were separately dissolved in deionized water. Similarly, the $BaFe_{12}O_{19}$ solution, so-called solution 2, was prepared by dissolving 1 M of each of the raw materials ($FeCl_3.6H_2O$) and ($BaCl_2.2H_2O$) in deionized water. NiO (solution 3) was also prepared by dissolving 1 M of ($NiCl_2.6H_2O$) in deionized water. The three separate solutions were magnetically stirred for one hour at room temperature to attain homogenized solutions. 3M Sodium hydroxide solution (NaOH) was added to $Ni_{0.5}Zn_{0.5}Fe_2O_4$ to attain a pH of 12, then heated at 80 °C for 2 h. While, 4 M Sodium hydroxide solutions (NaOH), were added dropwise to $BaFe_{12}O_{19}$ and NiO solutions until the pH was adjusted to 13, and then heated for two hours at 80 °C and 60 °C for solutions 2 and 3, respectively. The NiO sample was washed with deionized water, while the two ferrite samples were washed using a mixture of 75% deionized water and 25% ethanol to remove alkalinity and reduce the pH to 7. The three precipitates were dried at 100 °C for 16 h, followed by manual grinding with a pestle and mortar. Finally, the three pure nanopowders were calcined at 950 °C for 4 h.

2.2 Preparation of the ternary nanocomposites

The aim of using ball milling is to synthesize the following four ternary nanocomposites: C1($0.33NiO$, $0.33BaFe_{12}O_{19}$, $0.33Ni_{0.5}Zn_{0.5}Fe_2O_4$), C2($0.66NiO$, $0.166BaFe_{12}O_{19}$, $0.166Ni_{0.5}Zn_{0.5}Fe_2O_4$), C3($0.166NiO$,

$0.66BaFe_{12}O_{19}$, $0.166Ni_{0.5}Zn_{0.5}Fe_2O_4$), and C4($0.166NiO$, $0.166BaFe_{12}O_{19}$, $0.66Ni_{0.5}Zn_{0.5}Fe_2O_4$). The used nanoparticles NiO, $Ni_{0.5}Zn_{0.5}Fe_2O_4$, and $BaFe_{12}O_{19}$ have respective sizes of 48.46, 57.48, and 41.48 nm. Different weight percentages of the three nanoparticles were ball milled in the presence of absolute ethanol with a 5:1 ball-to-powder weight ratio at a fixed speed of 300 rpm for 10 min to obtain C1, C2, C3, and C4. In a muffle furnace, the four nanocomposites are calcined at 950 °C for 4 h at a rate of 5 °C per minute. Table 1 summarizes the compositions of the four ternary nanocomposites.

2.3 Characterization techniques

The structural parameters of the pure samples and the nanocomposites were investigated by the X-ray powder diffraction technique using a Bruker D8 Advance powder diffractometer with Cu-K_α radiation ($\lambda = 1.54056$ Å) in the range of $20° \leq 2\theta \leq 80°$. Furthermore, the morphology was examined using a JEOL JEM-100 CX transmission electron microscope (TEM) operated at 80 kV. The high-resolution transmission electron microscope (HRTEM) images were obtained using a JEM-2100 plus electron microscope. The X-ray photoelectron spectroscopy (XPS) measurements were performed via K-Alpha (ThermoFisher Scientific, USA) with monochromatic X-ray Alk$_\alpha$ radiation. The vibrating sample magnetometer (VSM, Lake Shore 7410) was used to conduct a magnetic study at room temperature under a maximum field of 20 kG.

Table 1 Experimental, fitted percentages, and crystallite sizes (D_{XRD} and D_{TEM}) calculated for the pure NiO, $Ni_{0.5}Zn_{0.5}Fe_2O_4$, $BaFe_{12}O_{19}$ and the nanocomposites (C1 to C4)

	Phases	Samples						
		NiO	$Ni_{0.5}Zn_{0.5}Fe_2O_4$	$BaFe_{12}O_{19}$	C1	C2	C3	C4
Experimental percentages (%)	NiO phase	100	–	–	33.3	66.6	16.6	16.6
	$BaFe_{12}O_{19}$ phase	–	–	100	33.3	16.6	66.6	16.6
	$Ni_{0.5}Zn_{0.5}Fe_2O_4$ phase	–	100	–	33.3	16.6	16.6	66.6
Fitted percentages (%)	NiO phase	100.00 ± 0.00	–	–	20.65 ± 0.36	63.74 ± 0.37	2.28 ± 0.66	13.34 ± 0.43
	$BaFe_{12}O_{19}$ phase	–	–	78.58 ± 0.00	6.32 ± 0.42	0.28 ± 0.10	36.49 ± 0.54	0.83 ± 0.13
	(Ni, Zn, Ba) Fe_2O_4 phase	–	100.00 ± 0.00	–	65.41 ± 0.46	35.96 ± 0.32	58.28 ± 0.63	85.81 ± 0.46
	α-Fe_2O_3 phase	–	–	21.41 ± 0.52	7.60 ± 0.40	---	2.93 ± 0.38	---
	χ^2	1.64	1.24	1.32	1.07	1.15	1.19	1.03
D_{XRD} (nm)	NiO phase	48.46	–	–	32.75	40.76	28.38	28.75
	$BaFe_{12}O_{19}$ phase	–	–	41.48	31.75	32.64	33.6	32.68
	(Ni, Zn, Ba) Fe_2O_4 phase	–	57.48	–	26.55	27.76	27.54	33.02
D_{TEM} (nm)		60.9	66.7	68	30.03	38.2	28.24	30.89

3 Results and discussion

3.1 X-ray powder diffraction (XRD)

Figure 1 shows the XRD patterns of pure NiO, $Ni_{0.5}Zn_{0.5}Fe_2O_4$, and $BaFe_{12}O_{19}$ nanophases with their Rietveld refinements performed using the MAUD software (acronym of Material Analysis Using Diffraction). Figure 2a–d show the experimental and the refined XRD patterns, as well as the exported Maud spectra of the constituent components of the nanocomposites C1, C2, C3, and C4, respectively. The fitted results are reported in Table 1 which shows a reliability factor χ^2 of the Rietveld refinements with a value close to unity, suggesting a good refinement. Pure NiO without any secondary phases is successfully formed and diffraction peaks of NiO are found at $2\theta = 37.24°$ 43.28°, 62.85°, 75.39° and 79.37° (Fig. 1) which correspond to the crystallographic planes (111), (200), (220), (311), and (222),
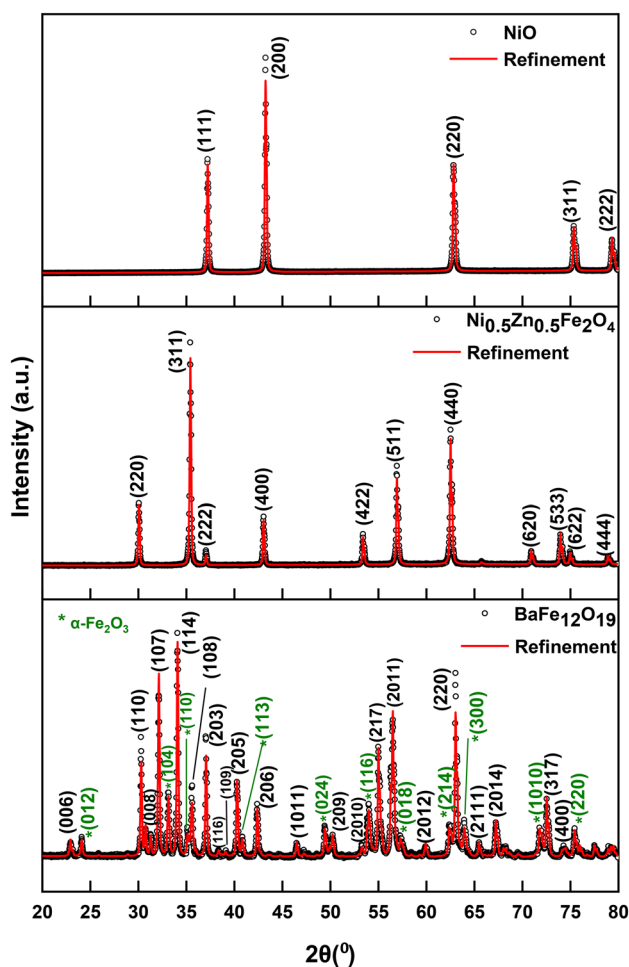
respectively. All the peaks match the ICDD card number 01–089-3080. The synthesis of high crystalline nanoparticles of the fcc phase with space group Fm3m was confirmed by the high peak intensities and positions [31]. Likewise, pure $Ni_{0.5}Zn_{0.5}Fe_2O_4$ nanophase shows the main diffraction peaks appearing at 30.09°, 35.44°, 43.08°, 53.44°, 56.97°, and 62.55° (Fig. 1) corresponding to the crystal planes (220), (311), (400), (422), (511) and (440), respectively. All the previous diffraction peaks are well-matched according to the standard spinel cubic structure [16] of $Ni_{0.5}Zn_{0.5}Fe_2O_4$ space group: Fd3m. The Maud fitting of NiO and $Ni_{0.5}Zn_{0.5}Fe_2O_4$ shows the formation of the pure samples without any additional secondary phases (Table 1). Moreover, the diffraction peaks for pure $BaFe_{12}O_{19}$ (Fig. 1) are in good agreement with its hexagonal magnetoplumbite structure of space group P63/mmc according to the (JCPDS: 43-0002). Peaks of the alpha hematite (α-Fe_2O_3, JCPDS: 24-0081) (marked with (*) in Fig. 1) are also present in the pattern of pure $BaFe_{12}O_{19}$ [15]. The fitting of $BaFe_{12}O_{19}$ shows that the α-Fe_2O_3 phase is produced with approximately 21.41%, while the pure $BaFe_{12}O_{19}$ with 78.58% as shown in Table 1. The formation of α-Fe_2O_3 could be due to the use of a stoichiometric amount of barium. According to Xu et al. [32], using too much barium rather than stoichiometric amounts will result in the formation of $BaFe_2O_4$, another intermediate phase, which is not formed in the current hard ferrite $BaFe_{12}O_{19}$. The characteristic peaks of the three pure nanophases (NiO, $BaFe_{12}O_{19}$, and $Ni_{0.5}Zn_{0.5}Fe_2O_4$) are present in the XRD patterns of C1, C2, C3, and C4 (Fig. 2a–d), and are designated with (#), (▲), and (+), respectively. And the secondary phase of α-Fe_2O_3 highlighted with (*) is also formed in some nanocomposites (C1 and C3). This confirms the successful formation of oxide/hard/soft ferrite nanocomposites. The importance of the exported spectra of the constituent phases (NiO, $BaFe_{12}O_{19}$, $Ni_{0.5}Zn_{0.5}Fe_2O_4$, and α-Fe_2O_3) of the NCs (Fig. 2a–d) is to clarify the phases to which each peak in the nanocomposites belong and to detect the overlapped peaks. In the spectrum of the nanocomposite C1 (Fig. 2a), peaks of NiO and $Ni_{0.5}Zn_{0.5}Fe_2O_4$ predominate, which reflect their high fitted percentages (Table 1). The main peak of pure $BaFe_{12}O_{19}$, which corresponds to the plane (114), may be seen at 34.130° in C1 spectrum but with very small intensity. Additionally, the peaks that correspond to the planes (107), (205), and (217), which are regarded as notable peaks in pure $BaFe_{12}O_{19}$, each showed in C1 at 32.143°, 40.307°, and 55.002° with extremely low intensities. This is due to the low content of $BaFe_{12}O_{19}$ (6.32%) found in C1 as seen in Table 1. Peaks of α-Fe_2O_3 are also visible in the spectrum of C1 separately at 23.925° and overlapping with other components at 53.692° and 57.244°. Moreover, in the spectrum of C2 (Fig. 2b), the NiO main peak, with a small contribution from the soft ferrite peak, is what makes up the highest peak at 43.264°. Similarly, the three peaks at 37.235°, 62.837°,

Fig. 1 Experimental and refined XRD patterns of pure NiO, $Ni_{0.5}Zn_{0.5}Fe_2O_4$, and $BaFe_{12}O_{19}$
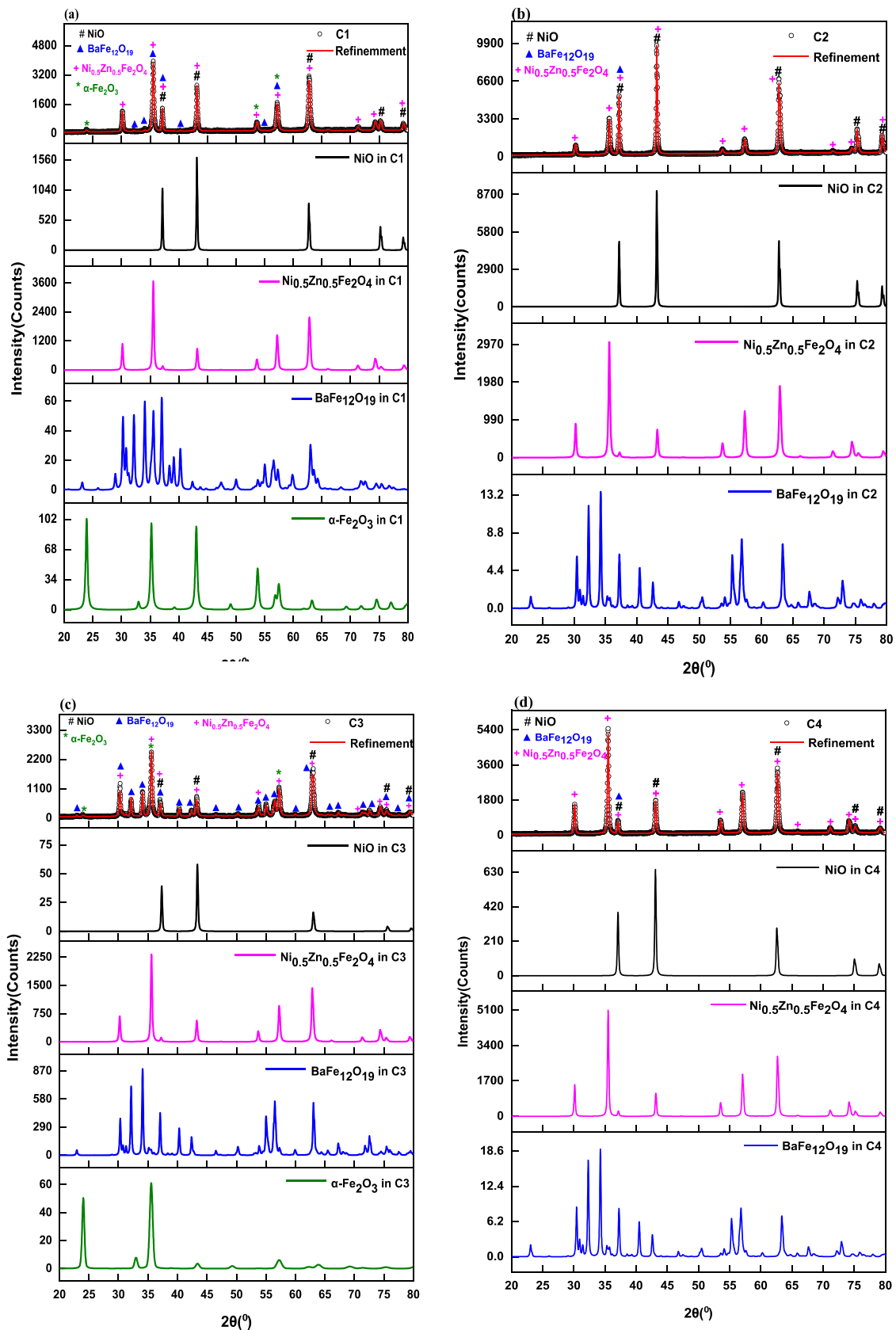
Fig. 2 Experimental, refined XRD patterns, and exported Maud spectra of the constituent components of **a** C1, **b** C2, **c** C3, and **d** C4

and 79.337° are made up of NiO as a primary component followed by $Ni_{0.5}Zn_{0.5}Fe_2O_4$. This information is consistent with the percentages in Table 1 which show that NiO makes up the majority (63.74%) and $Ni_{0.5}Zn_{0.5}Fe_2O_4$ comes in second place (35.96%). The $BaFe_{12}O_{19}$ peaks overlap with the other components and appear at 37.235° with very low intensity. Due to their extremely low intensities, the two primary peaks of pure $BaFe_{12}O_{19}$ at 32.307° and 34.252°, which correspond to the planes (107) and (114), are invisible in the spectrum of C2. Still, they are detected in the individual spectrum of $BaFe_{12}O_{19}$, as shown in Fig. 2b. These low peaks are consistent with the $BaFe_{12}O_{19}$ traces (0.28%) shown in Table 1. Likewise, the two main $BaFe_{12}O_{19}$ peaks can be seen in the C3 spectrum (Fig. 2c) at 34.11° and 32.17°, which correspond to the planes (114) and (107), respectively. Additionally, there are noticeable peaks of pure $BaFe_{12}O_{19}$ at 40.33°, 42.41°, 55.06°, and 56.56° which correspond to the planes (205), (206), (217), and (2011), respectively. This distribution of the $BaFe_{12}O_{19}$ peaks is consistent with the considerable amount of $BaFe_{12}O_{19}$ (34.13%) present in C3 as shown in Table 1. Moreover, the $Ni_{0.5}Zn_{0.5}Fe_2O_4$ major peak plus a very minor contribution from the α-Fe_2O_3 phase form the primary peak of C3 at 35.62°. The other $Ni_{0.5}Zn_{0.5}Fe_2O_4$ peaks may be seen throughout the C3 spectrum, indicating that the C3 nanocomposite contains a significant amount of soft phase (58.28%). Contrary, due to the low concentration of NiO (2.28%) in C3, all NiO peaks are visible in the C3 spectrum, but they are extremely faint and overlap as can be seen in Fig. 2c where the spectrum of NiO has low intensity. Moreover, all the $Ni_{0.5}Zn_{0.5}Fe_2O_4$ peaks dominate the C4 XRD spectrum (Fig. 2d), while the five NiO peaks are small and overlap with the $Ni_{0.5}Zn_{0.5}Fe_2O_4$ peaks. At 37.089°, there is only one peak for $BaFe_{12}O_{19}$ that appears to overlap with the other elements; but the whole spectrum of $BaFe_{12}O_{19}$ appears in Fig. 2d exhibiting a very small intensity consistent with the extremely low

concentration of $BaFe_{12}O_{19}$ (0.83%) present in C4. It can be noticed that in Fig. 2a–d the peak intensity for the spectrum of each component in the four nanocomposites is consistent with their percentages in Table 1. The decreased percentages of $BaFe_{12}O_{19}$ and NiO in all the nanocomposites (Table 1) may be attributed to the reaction of NiO with $BaFe_{12}O_{19}$ to create $NiFe_2O_4$. Due to its overlap with the peaks of $Ni_{0.5}Zn_{0.5}Fe_2O_4$, $NiFe_2O_4$ cannot be identified independently in the nanocomposites' Maud fitted spectra, but its existence increased the fitted percentage of the soft phase. Another explanation for the decline in the percentages of NiO and $BaFe_{12}O_{19}$ is the disintegration of $BaFe_{12}O_{19}$ into Barium atoms and α-Fe_2O_3, and their inclusion in the $Ni_{0.5}Zn_{0.5}Fe_2O_4$ phase in addition to NiO phase to generate $(Ni, Zn, Ba)Fe_2O_4$, which raises the proportion of the soft phase in all NCs. These two hypotheses are supported by the lack of secondary phases of BaO_2, $BaCO_3$, $BaFe_2O_4$, $Ba_2Fe_6O_{11}$, or any other secondary phases that could occur in such nanocomposites as described in the literature [33–35]. Moreover, the lattice parameters for $BaFe_{12}O_{19}$ (a and c), NiO (a), and $Ni_{0.5}Zn_{0.5}Fe_2O_4$ (a) were calculated using the fitted spectra obtained from the Maud software for each phase in the pure and nanocomposite samples, according to the following equations, respectively [16]:

$$d_{hkl} = \left(\frac{4}{3} \frac{h^2 + hk + k^2}{a^2} + \frac{l^2}{c^2} \right)^{-0.5} \tag{1}$$

$$a = d_{hkl} \left(h^2 + k^2 + l^2 \right)^{0.5} \tag{2}$$

where d_{hkl} and (hkl) are the crystal interplanar distance and the Miller indices respectively. The values of the lattice parameters are listed in Table 2. The lattice parameters of the three pure samples, nickel oxide, spinel, and hexagonal ferrites, are consistent with the standard values mentioned

Table 2 Lattice parameters calculated from XRD and SAED techniques for the three pure samples and the nanocomposites

Phases	Lattice parameters (XRD)				Lattice parameters (SAED)			
	a=b=c (Å)		a=b (Å)	c (Å)	a=b=c (Å)		a=b (Å)	c(Å)
	Samples							
	NiO phase	(Ni, Zn, Ba)Fe$_2$O$_4$ phase	BaFe$_{12}$O$_{19}$ phase	BaFe$_{12}$O$_{19}$ phase	NiO phase	(Ni, Zn, Ba)Fe$_2$O$_4$ phase	BaFe$_{12}$O$_{19}$ phase	BaFe$_{12}$O$_{19}$ phase
NiO	4.175	–	–	–	4.182	–	–	–
Ni$_{0.5}$Zn$_{0.5}$Fe$_2$O$_4$	–	8.388	–	–	–	8.393	–	–
BaFe$_{12}$O$_{19}$	–	–	5.895	23.176	–	–	5.890	23.254
C1	4.183	8.361	5.931	23.217	4.178	8.382	5.856	23.862
C2	4.180	8.350	5.867	23.120	4.183	8.359	5.861	23.76
C3	4.180	8.356	5.895	23.200	4.181	8.352	5.998	23.306
C4	4.198	8.376	5.867	23.081	4.177	8.363	5.903	23.324

in previous literature [31, 36, 37]. However, their values in the nanocomposites show small deviations. This can be due to the effects of surface compression of the oxide, soft, and hard phases [38]. Additionally, the crystallite sizes (D_{XRD}) of the three pure nano-samples (NiO, $Ni_{0.5}Zn_{0.5}Fe_2O_4$, and $BaFe_{12}O_{19}$), as well as the constituent phases of the nano-composites (C1 to C4), were calculated using the well-known Debye Scherrer equation Table 1 lists the results of the crystallite sizes. The crystallite sizes of all three pure nanophases are greater than those of the corresponding nanocomposite phases. This decrease in crystallite size in nanocomposites indicated a high surface-to-volume ratio [39]. For the nanocomposites, the crystallite size for NiO increases with increasing its percentages according to Maud fitted data thus indicating an improvement in its crystallinity [40]. It is noticeable that $BaFe_{12}O_{19}$ in C3 and (Ni, Zn, Ba)Fe_2O_4 in C4 both show the largest crystallite sizes when compared to their sizes in the other nanocomposites, which is not surprising given that $BaFe_{12}O_{19}$ and (Ni, Zn, Ba)Fe_2O_4 make up the highest percentages in C3 and C4, respectively. One can conclude that the presence of (Ni, Zn, Ba)Fe_2O_4 and $BaFe_{12}O_{19}$ in the nanocomposites in the highest percentages facilitated the growth of these phases and improved their crystallinity. Additionally, the crystallite sizes of (Ni, Zn, Ba)Fe_2O_4 and $BaFe_{12}O_{19}$ in nanocomposites other than C4 and C3, respectively, are unaffected by their weight percentages and do not change significantly. This is most likely because the calcination temperature (950 °C) is the same for all samples [41].

3.2 Transmission electron microscopy (TEM) and selected area electron diffraction (SAED)

Figure 3Ia–g depict the TEM micrographs of pure NiO, $Ni_{0.5}Zn_{0.5}Fe_2O_4$, $BaFe_{12}O_{19}$, and the nanocomposites C1, C2, C3, and C4, respectively. The TEM image of pure NiO (Fig. 3Ia) shows a cubic shape with different grain sizes. While $Ni_{0.5}Zn_{0.5}Fe_2O_4$ (Fig. 3Ib) exhibits agglomerated nanoparticles with quasi-spherical morphology. Additionally, $BaFe_{12}O_{19}$ (Fig. 3Ic) shows different sizes and shapes of hexagonal nanoparticles. Nearly spherical nanoparticles of α-Fe_2O_3 are noticed in the TEM image of $BaFe_{12}O_{19}$ (Fig. 3Ic) which agrees with XRD fitted data (Table 1). Similar hexagonal and spherical morphologies were observed for $BaFe_{12}O_{19}$ and α-Fe_2O_3 nanoparticles, respectively, in the previous literature [42, 43]. In the nanocomposites, different morphologies, in agreement with XRD fitted data, corresponding to different nanophases can be distinguished as it is shown in Fig. 3Id–g. The mean grain sizes (D_{TEM}) calculated from the TEM images of the pure samples and the nanocomposites are listed in Table 1. Additionally, few nanoparticles are separated and most of them are agglomerated. This phenomenon shows that the nanoparticles in pure

and nanocomposite samples have significant magnetic dipole interactions among them [44]. The highest agglomeration was observed in C3 among the other three nanocomposites. The shapes of pure nanoparticles were confirmed and labeled in Fig. 3Id–g. In the TEM image of C2 (Fig. 3Ie), the dominant NiO phase displays an identifiable cubic morphology. For a better inspection of the microstructure of the samples, the selected area electron diffraction (SAED) images for the pure and the nanocomposite samples are studied. Figure 3IIa–g illustrate the SAED images of pure NiO, $Ni_{0.5}Zn_{0.5}Fe_2O_4$, $BaFe_{12}O_{19}$ and the nanocomposites C1, C2, C3, and C4, respectively. Concentric circles may be seen in SAED patterns, which indicate the samples' polycrystalline nature. Using image J software to calculate the d-spacing from the ring pattern, the samples' crystal structure was analyzed. The (hkl) planes are indexed as indicated in Fig. 3IIa–g as the values of the d-spacing obtained from the SAED pictures were found to be comparable with those obtained from XRD measurements for pure samples and NCs. The lattice constants of the pure samples and the constituent phases of the NCs were evaluated from the obtained SAED d-spacing values using Eqs. (1) and (2), and their values are listed in Table 2. These values are found to fall within the same range as those calculated from XRD measurements. Additionally, a correlation between the planes provided in SAED images (Fig. 3IIa–g) and the phases displayed in TEM images (Fig. 3Ia–g) can be noticed for most pure samples and NCs.

3.3 X-ray photoelectron spectroscopy (XPS)

The oxidation states of the existing elements in the pure and nanocomposite samples are identified using the XPS measurements. The XPS survey spectra of NiO, $Ni_{0.5}Zn_{0.5}Fe_2O_4$, $BaFe_{12}O_{19}$, C1, and C3 are shown in Fig. 4. The survey spectrum of pure NiO shows the presence of Nickel and Oxygen. While the $Ni_{0.5}Zn_{0.5}Fe_2O_4$ survey spectrum demonstrates the presence of Nickel, Zinc, Iron, and Oxygen. Also, the XPS spectrum of pure $BaFe_{12}O_{19}$ depicts the main peaks of Barium, Iron, and Oxygen. Traces of carbon appear in the spectra of all pure and NCs due to the exposure of the samples to air before the XPS measurements [45]. Moreover, the nanocomposites C1 and C3 show a combination of the pure phases NiO, $Ni_{0.5}Zn_{0.5}Fe_2O_4$, and $BaFe_{12}O_{19}$. As a result, C1 and C3 contain Nickel, Zinc, Barium, Iron, Oxygen, and Carbon peaks. Consequently, the XPS results show that the synthesized pure samples and nanocomposites are successfully formed, which supports the XRD results. Additionally, the main spectral lines of nickel, zinc, iron, barium, and oxygen are collected using the high-resolution XPS measurements and deconvoluted, as depicted in Fig. 5a–e, respectively. Figure 5a displays the deconvoluted Ni-2p spectral lines in NiO, $Ni_{0.5}Zn_{0.5}Fe_2O_4$, C1, and C3.

(I)
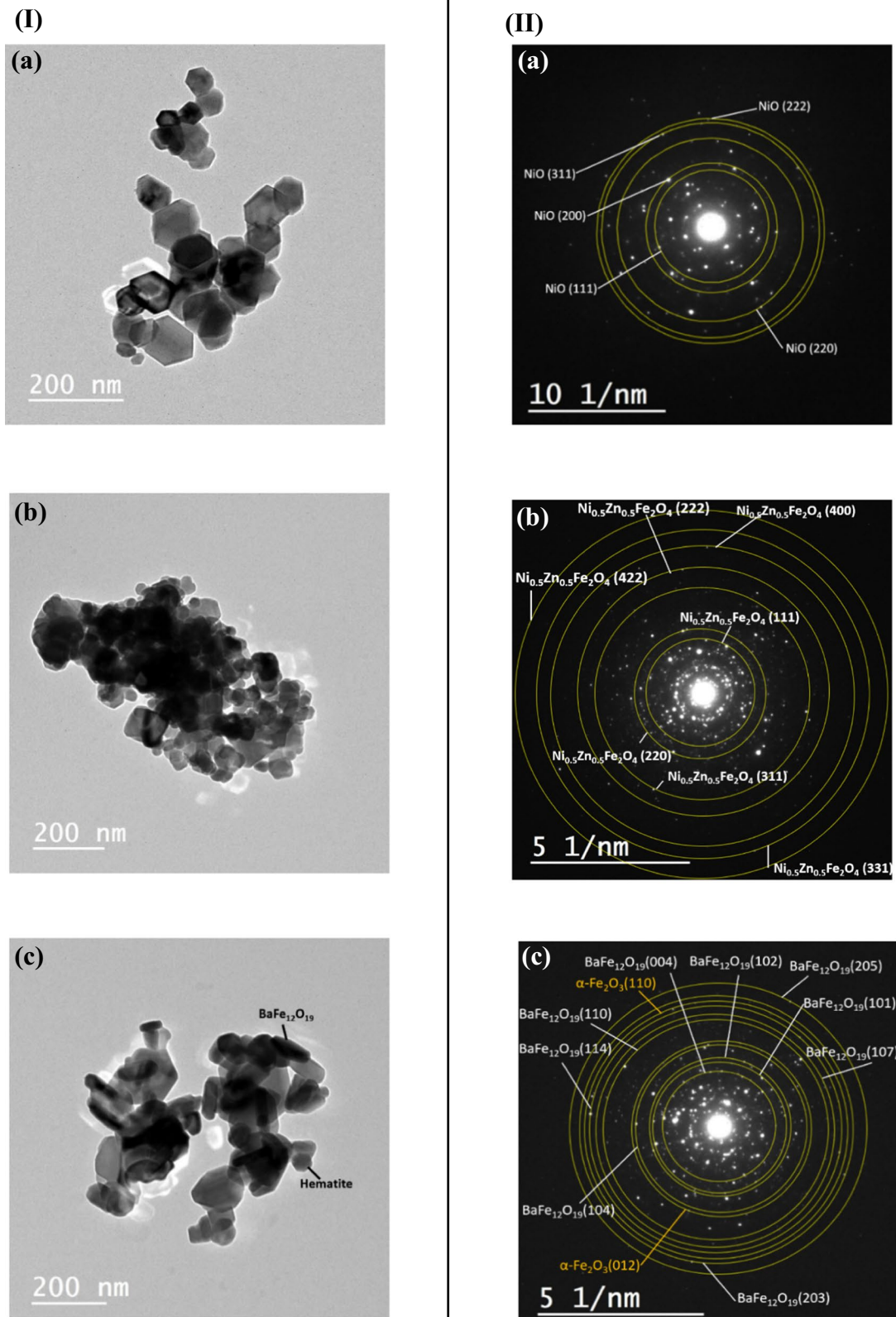**(a)**

(II)
(a)

(b)

(b)

(c)

(c)

Fig. 3 TEM micrographs (**I**) and SAED images (**II**) of **a** pure NiO, **b** pure $Ni_{0.5}Zn_{0.5}Fe_2O_4$, and **c** pure $BaFe_{12}O_{19}$ and the nanocomposites, **d** C1, **e** C2, (**f**) C3, and **g** C4
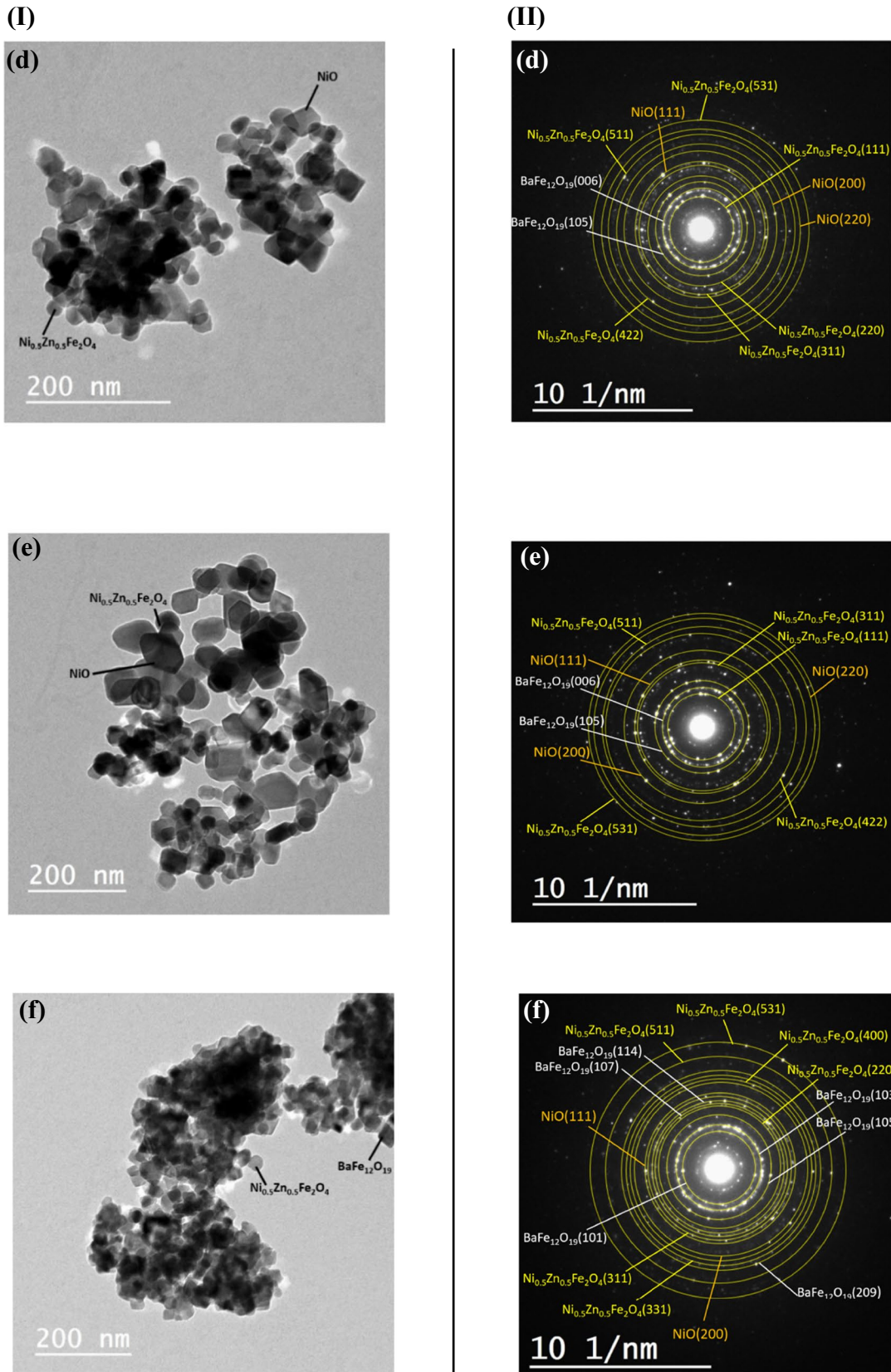
(I)

(II)

Fig. 3 (continued)

(I)

(II)

Fig. 3 (continued)

The nickel spin–orbit doublets (Ni-$2p_{3/2}$ and Ni-$2p_{1/2}$) are present in the four spectra and split into many peaks because of the nickel's distinct oxidation states. The four deconvoluted XPS spectra also demonstrate Ni^{2+} and Ni^{3+} oxidation

Fig. 4 The XPS spectra of NiO, $Ni_{0.5}Zn_{0.5}Fe_2O_4$, $BaFe_{12}O_{19}$, C1, and C3

states that are connected via satellites at higher binding energies. The values of the binding energies for the different oxidation states of the elements are tabulated in Table 3. The values of Ni-2p binding energy are in good agreement with the literature [46, 47]. According to Fig. 5b, there are two prominent peaks in the high-resolution XPS spectra of zinc (Zn-2p) in $Ni_{0.5}Zn_{0.5}Fe_2O_4$, C1, and C3 NCs that are centered around 1021 and 1044 eV and are assigned to Zn-$2p_{3/2}$ and Zn-$2p_{1/2}$, respectively, indicating that zinc is in the +2 oxidation state [48]. Additionally, all samples exhibit the two principal Fe-2p spin–orbit doublet peaks (Fe-$2p_{3/2}$ and Fe-$2p_{1/2}$), which have binding energies of around 710 and 724 eV, respectively, shown in Fig. 5c. Furthermore, the deconvoluted spectra of Fe-2p peaks reveal the presence of Fe^{3+} in the octahedral (O_h) and tetrahedral (T_h) locations. Also, satellite peaks that can be attributed to a shake-up were found at higher binding energies in the two spin–orbit doublet peaks. The positions of the deconvoluted Fe-$2p_{3/2}$ and Fe-$2p_{1/2}$ peaks listed in Table 3 are comparable to the studies done in the previous literature [13, 49, 50]. As shown in Fig. 5d, the high-resolution XPS spectra of barium (Ba-3d) in $BaFe_{12}O_{19}$, C1, and C3 nanocomposites exhibit two prominent peaks with centers at 779 and 795 eV that are assigned to Ba-$3d_{5/2}$ and Ba-$3d_{3/2}$, respectively, confirming the presence of Ba^{2+} oxidation state [51]. On the other hand, the main spectral lines of Oxygen (O-1s) in the five samples are deconvoluted into two peaks that indicate the different kinds of O species as shown in Fig. 5e. The first deconvoluted peak is centered at 529 eV and can be assigned to the contribution from lattice oxygen (O_L). The second deconvoluted peak (O_v) centered at 531 eV can be attributed to the surface oxygen resulting from the oxygen vacancies present on the surfaces of the hexagonal and spinel ferrites [52].

Fig. 5 The deconvolution of the main spectral lines of **a** Ni-2p, ▶ **b** Zn-2p, **c** Fe-2p, **d** Ba-3d, and **e** O-1s of NiO, $Ni_{0.5}Zn_{0.5}Fe_2O_4$, $BaFe_{12}O_{19}$, C1, and C3

3.4 Vibrating sample magnetometer (VSM) analysis

Room temperature hysteresis loops are performed under a ($\pm$ 20 kG) applied field to study the magnetic characteristics of pure and nanocomposite materials via the VSM technique. Magnetic hysteresis (M-H) loops are recorded for the pure samples NiO, $Ni_{0.5}Zn_{0.5}Fe_2O_4$, $BaFe_{12}O_{19}$, and the nanocomposites (C1, C2, C3 and C4) which are depicted in Fig. 6Ia–c, II, respectively. The values of the saturation magnetization M_s, coercivity H_c, and remanent magnetization M_r extracted directly from the hysteresis curves are listed in Table 4. The M–H loop of NiO nanoparticles (Fig. 6Ia) shows an antiferromagnetic activity demonstrated by a lack of a saturated plateau region even at the high applied field of 20 kG. While the $Ni_{0.5}Zn_{0.5}Fe_2O_4$ M–H curve (Fig. 6Ib) shows a weak soft ferromagnetic behavior reaching M_s of 69.118 emu/g and a very small coercive field of H_c equals 8.819 G (shown in the inset of Fig. 6Ib). Furthermore, the $BaFe_{12}O_{19}$'s M–H loop (Fig. 6Ic) demonstrates a hard ferromagnetic behavior with a saturation magnetization (M_s) of 41.705 emu/g and a coercive field (H_c) of 4160.200 G. A small kink behavior is observed around low fields which can be due to the presence of α-Fe_2O_3 nanoparticles with a percentage of 21.41% approximately as confirmed from the XRD analysis (Table 1) [15]. Besides, C1, C2, and C4 all exhibit a ferromagnetic activity with varying M_s values (Fig. 6II). The two dominant phases in C1, C2, and C4 are NiO and (Ni, Zn, Ba)Fe_2O_4 according to XRD fitted data (Table 1) implying that interfacial exchange coupling between antiferromagnetic (AFM) NiO and the ferromagnetic (FM) (Ni, Zn, Ba)Fe_2O_4 phase are expected to significantly control the magnetic properties with a possible minor contribution from $BaFe_{12}O_{19}$ present in small amounts in these NCs [28, 53]. While, the nanocomposite C3 is considered a two-phase permanent magnet because of the coexistence of the hard magnetic $BaFe_{12}O_{19}$ (36.49%), and soft magnetic (Ni, Zn, Ba)Fe_2O_4 (58.28%). Additionally, the idea of combining three materials in a composite is to investigate the effect of interaction among them on different magnetic parameters. The highest weights percent of NiO (63.74%), $BaFe_{12}O_{19}$ (36.49%), and $Ni_{0.5}Zn_{0.5}Fe_2O_4$ (85.81%) are found in C2, C3, and C4, respectively. The different amounts of phases affect the values of M_s, M_r, and H_c in C2, C3, and C4. From Table 4, the arrangement of values of the magnetic parameters for pure NiO, $BaFe_{12}O_{19}$, and $Ni_{0.5}Zn_{0.5}Fe_2O_4$ are as follows: $M_s(NiO) = 0.204 < M_s(BaFe_{12}O_{19}) = 41.705 < M_s(Ni_{0.5}Zn_{0.5}Fe_2O_4) = 69.118$ emu/g, $M_r(NiO) = 0.010 < M_r(Ni_{0.5}Zn_{0.5}Fe_2O_4) = 0.643 < M_r(BaF$

a) Ni-2p
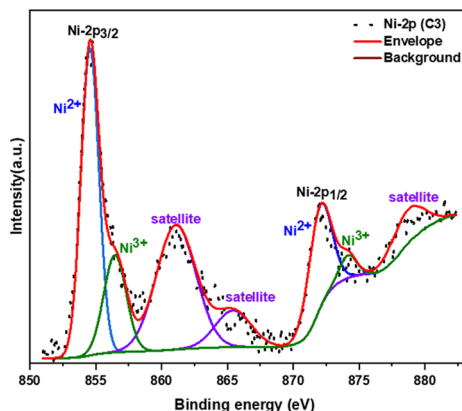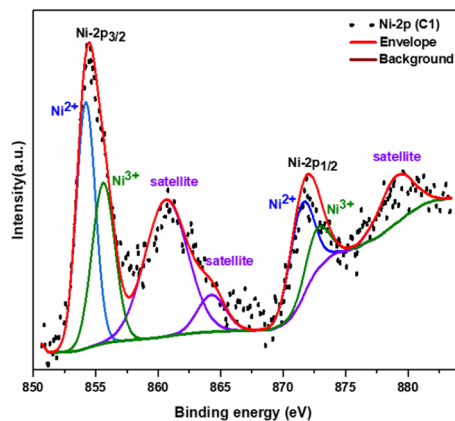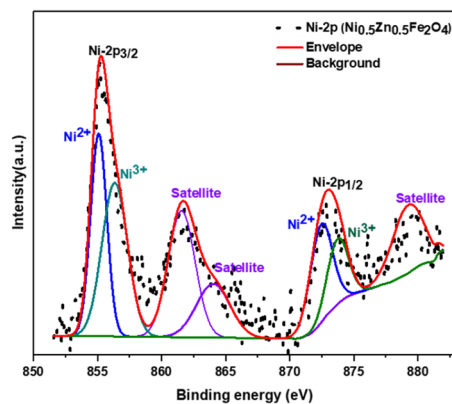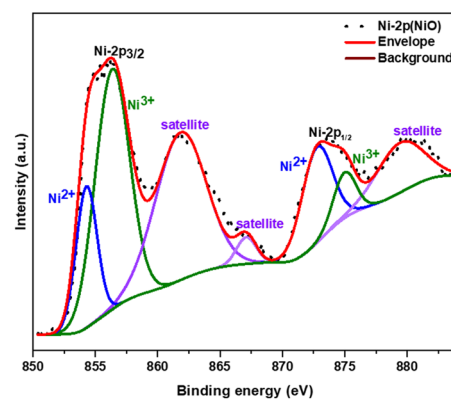
b) Zn-2p
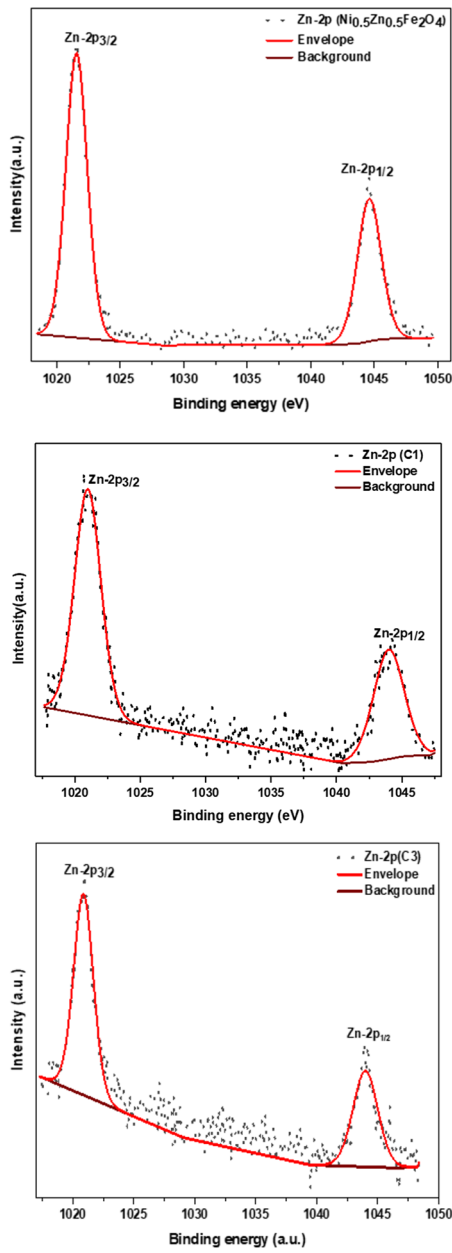
c) Fe-2p
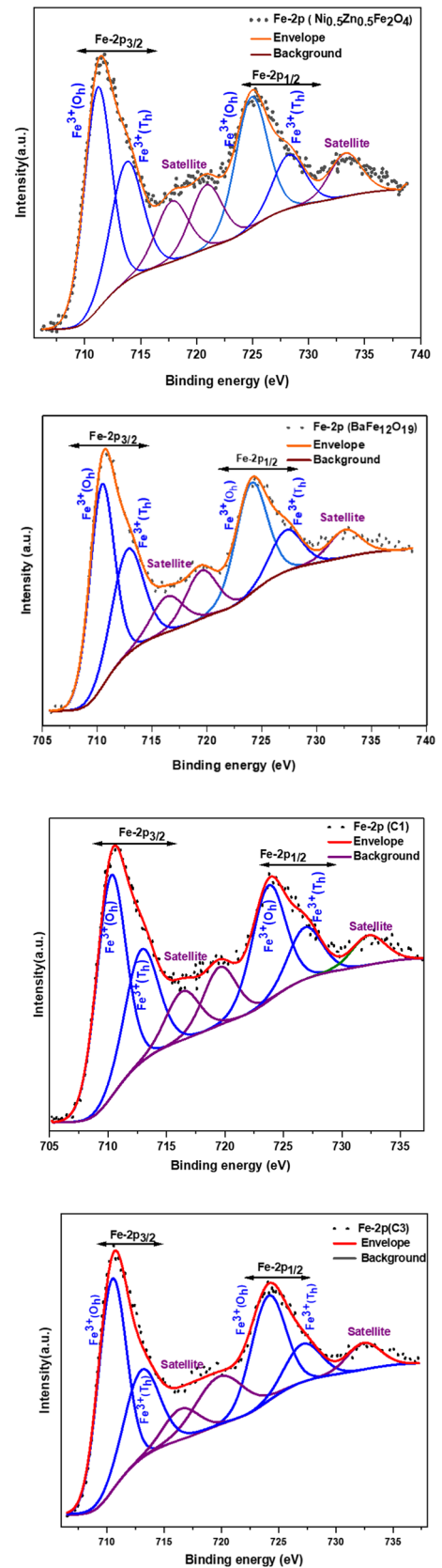
Fig. 5 (continued)

Fig. 5 (continued)

d) Ba-3d

e) O-1s

Fig. 5 (continued)

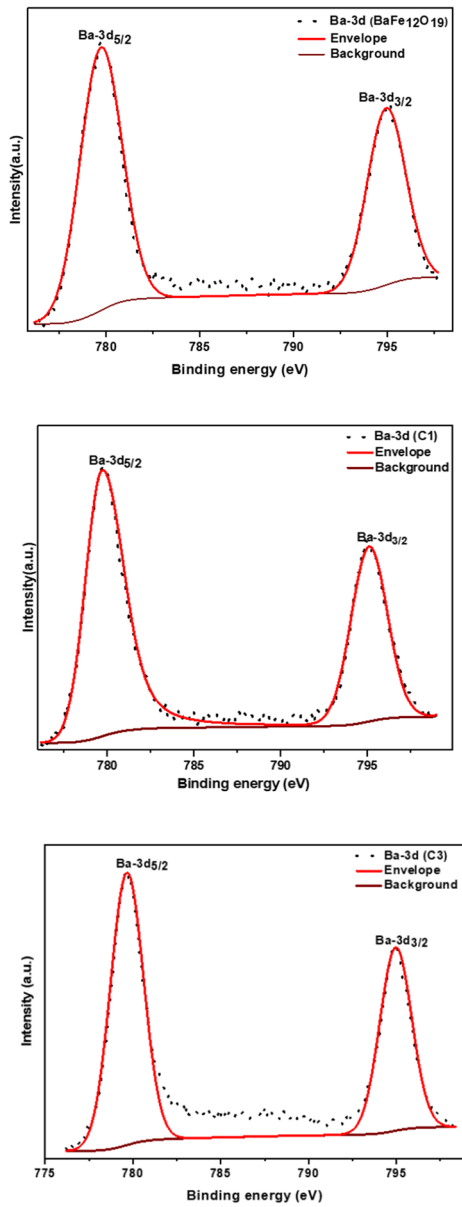**Fig. 5** (continued)

e) O-1s

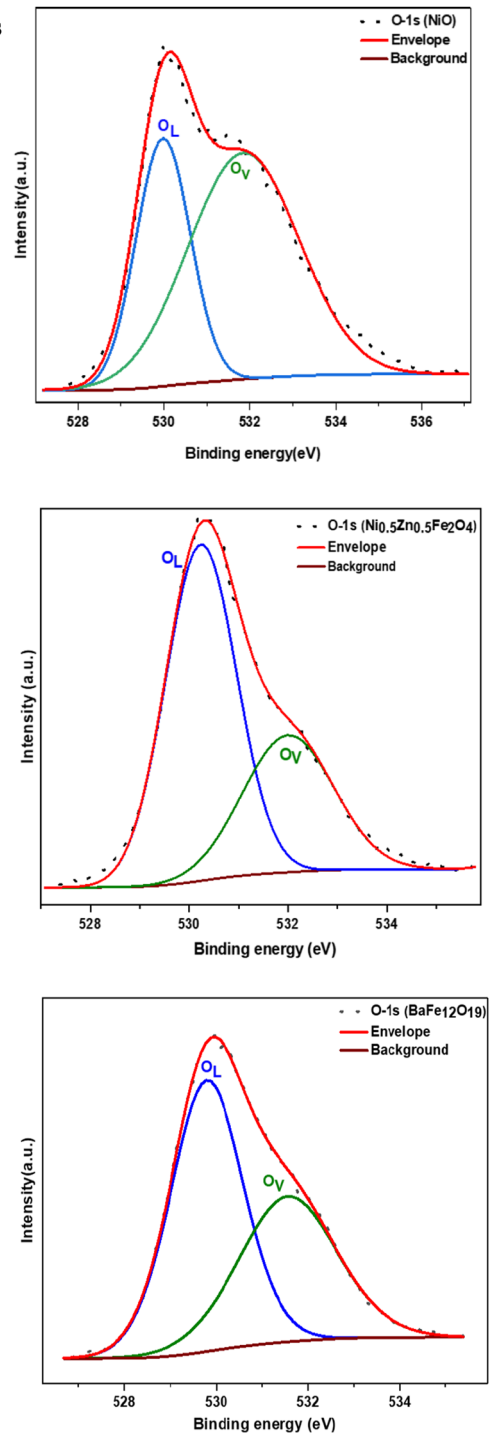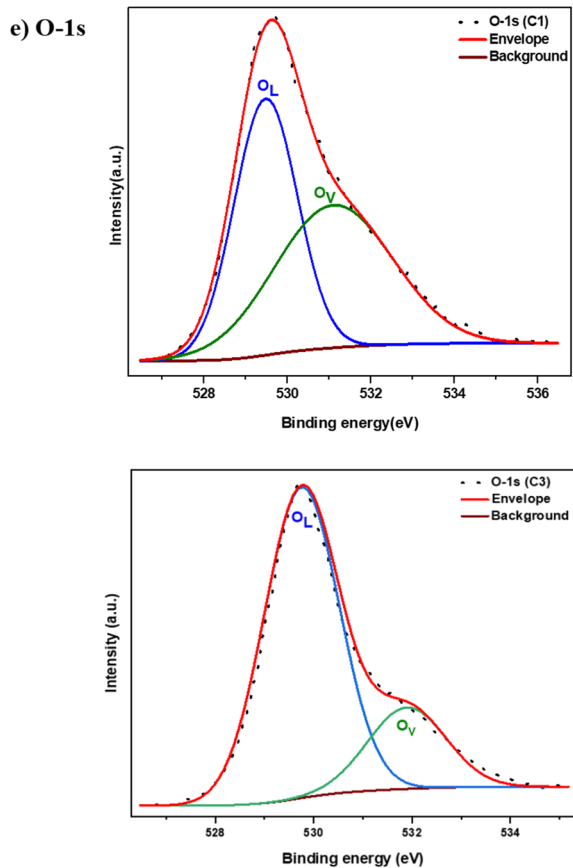**Fig. 5** (continued)

$e_{12}O_{19}) = 19.730$ emu/g, and $H_c(Ni_{0.5}Zn_{0.5}Fe_2O_4) = 8.819 < H_c(NiO) = 288.890 < H_c(BaFe_{12}O_{19}) = 4160.200$ G. These arrangements with the highest weight percent of each phase in the composites can be good indicators for the existence of the lowest and highest values of M_s, M_r and H_c in C2, C3 and C4. For C2 (NiO is dominant), the lowest values of M_s (16.566 emu/g) and M_r (2.513 emu/g) exist. The highest values of H_c(472.110 G) and M_r(13.308 emu/g) correspond to C3 ($BaFe_{12}O_{19}$ is dominant). Sample C4 ($Ni_{0.5}Zn_{0.m5}Fe_2O_4$ is dominant) includes the highest value of M_s(50.033 emu/g) and the lowest value of H_c(76.306 G). The lowest values of M_s in C2 with a dominant NiO phase can be due to the interaction of the dipoles of the AFM with the FM at the interface boundaries. The dipolar interaction between an FM particle and the large number of surrounding AFM particles lowers the overall magnetization of the nanocomposites leading to the lowest M_s (16.566 emu/g) in C2 [54]. Similarly, the drop in M_s in a nanocomposite can be attributed to the non-collinear spin arrangement at the interfaces of the oxide and ferrite phases [49]. Non-collinear spin arrangements disorder the alignment of magnetic moments between the FM and AFM phases and within the FM nanoparticles. The nanocomposite's overall magnetic moment can be reduced

due to the misalignment, causing a smaller M_s. The highest M_s (53.033 emu/g) is retained in the nanocomposite C4. This behavior can be explained by the interfacial interaction at the interface between FM and AFM. Two types of interactions can be considered to explain the high value of M_s: exchange coupling and exchange anisotropy. Alignment of magnetic moments of AFM and FM can be achieved by the exchange coupling. The antiparallel alignment can reduce M_s and the parallel alignment can increase the value of M_s (as in the case of the sample C4). On the other hand, the effect of the exchange anisotropy can affect the orientation of the ferromagnetic phase magnetization, which leads to an increase in M_s [55]. Due to the small weight percent of NiO (2.28%) in C3, the interface between soft and hard ferrites will be considered. There are two main interactions, exchange, and dipolar interactions that determine the magnetic properties in C3. Besides, three exchange energy terms must be considered: first, the exchange energy between the soft and the hard (which is dominant); second, the exchange energy between the soft and the soft; and third, the exchange energy between the hard and the hard [56]. However, the presence of the soft ferrite phase having a lower magnetocrystalline anisotropy along with the hard ferrite phase in a nanocomposite leads to an exchange-coupling interaction between soft and hard phases. This exchange-coupling causes the magnetic moments at the interface of the $BaFe_{12}O_{19}$/(Ni, Zn, Ba)Fe_2O_4 in C3 to deviate from the local easy axis and align parallel to one another, raising the magnetization value [55]. This spin alignment is what causes the M_s of C3 (49.993 emu/g) to be higher than that of the pure hard ferrite $BaFe_{12}O_{19}$ (41.705 emu/g). Because of the considerable anisotropy of the $BaFe_{12}O_{19}$, the magnetization reversal with a lower applied field becomes difficult to achieve leading to a very high H_c (4160.200 G) for pure $BaFe_{12}O_{19}$. Furthermore, the reason for the greatest H_c value of C3 compared to the other NCs can be explained as follows: The magnetization in soft grains of (Ni, Zn, Ba)Fe_2O_4 is prevented from reversing with the reversal of the applied field because of a significant exchange force acting on the magnetization that develops with an increase in the volume fraction of the hard magnetic $BaFe_{12}O_{19}$ phase. The presence of the soft grain in this region, however, prevents direct coupling between magnetization inside different hard grains, and the low value of the soft–soft exchange constant prevents indirect coupling through soft grains, which results in a weak coupling between the magnetization inside the various hard grains in this region [56]. When the inter-grain exchange coupling of the hard grains is weakened, their averaging effect of anisotropy is suppressed leading to an increased coercivity [57, 58]. Therefore, the increase in the percentages of hard phases increased the coercivity [56]. Moreover, because of the reduced anisotropy of the soft magnetic ferrite phase in C4, magnetization reversal can be easily attained with the

Table 3 The binding energy of the de-convoluted main spectral lines of NiO, $Ni_{0.5}Zn_{0.5}Fe_2O_4$, $BaFe_{12}O_{19}$, C1, and C3

Core energy levels		Assignment	NiO	$Ni_{0.5}Zn_{0.5}Fe_2O_4$	$BaFe_{12}O_{19}$	C1	C3
Ba-3d	Ba-3d$_{5/2}$	Ba^{2+}	–	–	779.78	779.78	779.68
	Ba-3d$_{3/2}$	Ba^{2+}	–	–	794.98	795.08	794.98
Ni-2p	Ni-2p$_{3/2}$	Ni^{2+}(O$_h$)	854.28	855.18	–	854.18	854.58
		Ni^{3+}(T$_h$)	856.38	856.98	–	855.68	856.48
		Satellite	861.98	861.78	–	860.68	861.08
		Satellite	867.18	865.68	–	864.28	865.48
	Ni-2p$_{1/2}$	Ni^{2+}(O$_h$)	872.98	872.98	–	872.08	872.18
		Ni^{3+}(T$_h$)	875.08	873.33	–	872.98	874.28
		Satellite	879.88	879.18	–	879.58	879.28
Zn-2p	Zn-2p$_{3/2}$	Zn^{2+}	–	1021.58	–	1020.98	1020.88
	Zn-2p$_{1/2}$	Zn^{2+}	–	1044.58	–	1044.08	1043.98
Fe-2p	Fe-2p$_{3/2}$	Fe^{3+}(O$_h$)	–	711.16	710.41	710.25	710.58
		Fe^{3+}(T$_h$)	–	713.73	712.76	712.86	713.18
		Satellite	–	717.8	716.37	716.38	716.78
		Satellite	–	720.87	719.49	719.56	720.18
	Fe-2p$_{1/2}$	Fe^{3+}(O$_h$)	–	724.88	724.02	723.73	724.28
		Fe^{3+}(T$_h$)	–	728.23	727.2	726.84	727.38
		Satellite	–	733.3	732.57	732.3	732.58
O-1s		O$_L$	529.98	530.28	529.8	529.48	529.78
		O$_V$	531.88	532.08	531.56	531.18	531.88

minimal applied field leading to the lowest H_c (76.306 G) in C4 [55].

The magnetic parameters such as the squareness ratio (SQR) and magnetocrystalline anisotropy constant (K) were evaluated [59] using Eqs. (3) and (4), respectively, then tabulated in Table 4.

$$SQR = \frac{M_r}{M_s} \tag{3}$$

$$K = \frac{H_c \times M_s}{0.98} \tag{4}$$

Squareness values around 0.50 and 0.831 are for non-interacting random nanoparticles with uniaxial and cubic anisotropies, respectively [60]. In the current work, the resulting squareness values for the prepared samples are below 0.5, which points to the uniaxial anisotropy contribution and magnetostatic interactions [54]. The high magnetocrystalline anisotropy is accompanied by the presence of a high percentage of the hard ferrite $BaFe_{12}O_{19}$ phase. This can be observed in C3 which has the highest $BaFe_{12}O_{19}$ content (36.49%) and exhibits the highest magnetocrystalline anisotropy (K=24.083 erg/g) while the lowest hard ferrite content in C2 (0.28 %) leads to the lowest anisotropy constant (1.753 erg/g). The well-smoothed hysteresis loops of C1, C2, and C4 (Fig. 6II) demonstrate that the oxide and

ferrite phases maintain inter-grain exchange coupling. The magnetization will produce a superimposition of two loops rather than a single loop if it is not exchange-coupled or weakly exchange-coupled [29]. On the other hand, the M-H loop of C3 (Fig. 6II) is not well-smoothed and displays a kink, indicating that the magnetization reversal cannot be completed in a single step and that these magnets have imperfect exchange coupling. Thus, in this case, when a magnetic field is introduced, both the hard and soft spins rotate independently [9]. In other words, both magnetic phases are switched separately as a result of this superimposition [41]. A common indication for investigating exchange coupling signs is switching field distribution (SFD), or dM/dH of the demagnetization curve shown in Fig. 7a–c for the pure nano-samples and the ternary nanocomposites C1, C2, C4, and C3, respectively. From Fig. 7a, pure $BaFe_{12}O_{19}$ and pure $Ni_{0.5}Zn_{0.5}Fe_2O_4$ show a major peak at $H_c = -6195.38$ G and a single high-intensity peak at $H_c = 148.397$ G, respectively. Similar values of H_c are reported by Yassine et al. [16] for pure $Ba_{0.5}Sr_{0.5}Fe_{12}O_{19}$ and $Ni_{0.5}Zn_{0.5}Fe_2O_4$ prepared by the co-precipitation method. The inset of Fig. 7a likewise depicts a single peak for NiO that is comparable to earlier research [61]. The nanocomposites C1, C2, and C4 in Fig. 7b also exhibit one sharp peak, showing that NiO and (Ni, Zn, Ba)Fe_2O_4 have a significant exchange coupling interaction. The nanocomposite C3 in Fig. 7c, demonstrates

Fig. 6 The M–H curves of (**I**) **a** pure NiO (The inset shows the magnification at lower fields), **b** pure $Ni_{0.5}Zn_{0.5}Fe_2O_4$ (The inset shows the magnification at lower fields), **c** pure $BaFe_{12}O_{19}$, (**II**) the nanocomposites C1, C2, C3, and C4
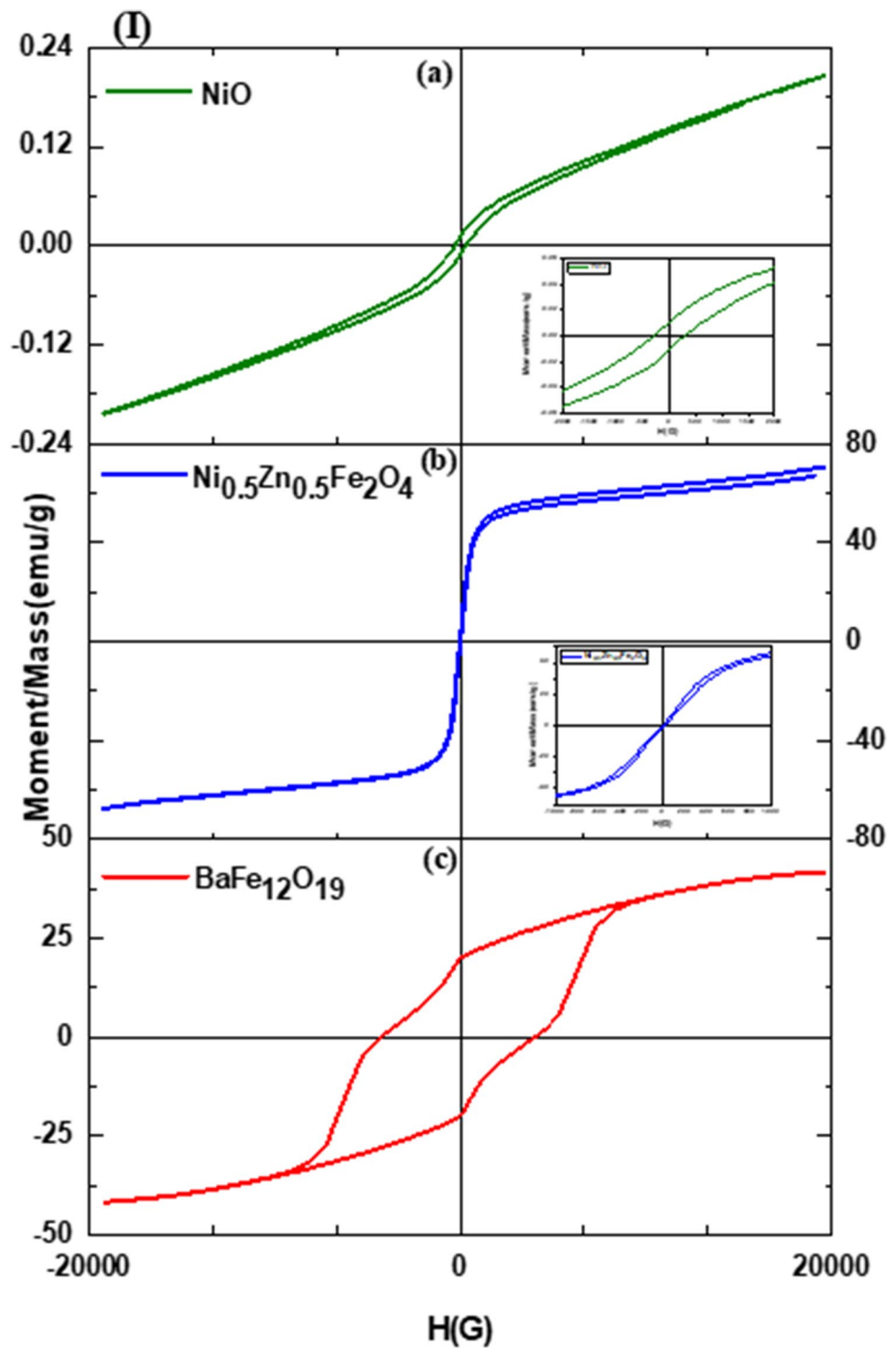
two peaks, one attributed to the hard phase and the other related to the soft phase. The appearance of two separate peaks in C3 indicates that a one-stage reversal of magnetization is not possible, and a weak exchange coupling effect is present [62]. Furthermore, the presence and strength of the exchange coupling interaction between the various magnetic phases in the produced nanocomposites are also studied using Henkel plots (δM, H), as shown by the following equation[63]:

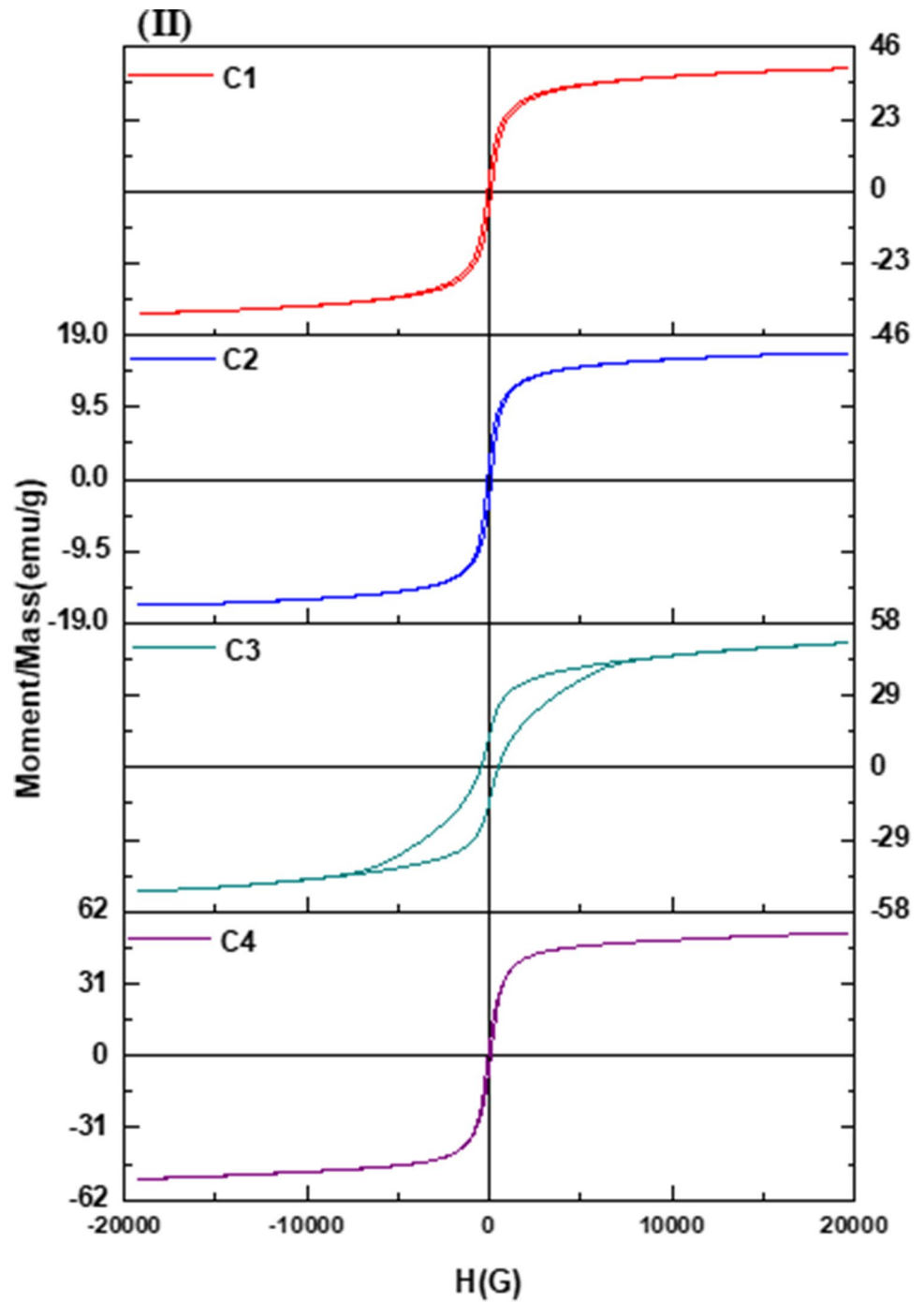$$\delta M = m_d(H) - [1 - 2m_r(H)] \tag{5}$$

Fig. 6 (continued)

Table 4 The observed (M_s, H_c, and M_r) and calculated (SQR and K) magnetic parameters of the pure samples and nanocomposites

	M_s (emu/g)	H_c (G)	M_r (emu/g)	SQR	$K \times 10^3$ (erg/g)
NiO	0.204	288.890	0.010	0.051	0.060
$Ni_{0.5}Zn_{0.5}Fe_2O_4$	69.118	8.819	0.643	0.009	0.621
$BaFe_{12}O_{19}$	41.705	4160.200	19.730	0.473	177.041
C1	39.052	107.940	5.032	0.128	4.301
C2	16.566	103.750	2.513	0.151	1.753
C3	49.993	472.110	13.308	0.266	24.083
C4	53.033	76.306	5.128	0.096	4.129
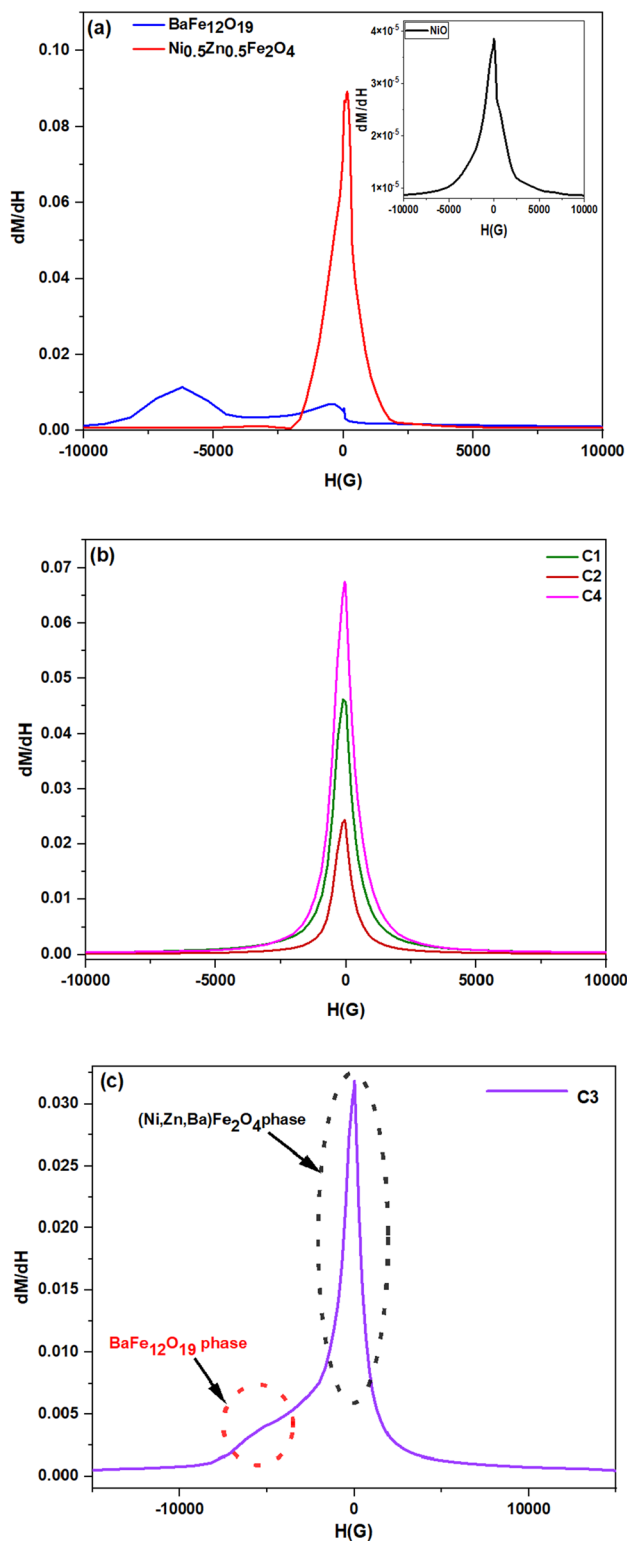
Fig. 7 dM/dH vs. H curves for **a** pure BaFe$_{12}$O$_{19}$ and Ni$_{0.5}$Zn$_{0.5}$Fe$_2$O$_4$ (the inset shows dM/dH vs. H curve for pure NiO), the nanocomposites **b** C1, C2 and C4 and **c** C3
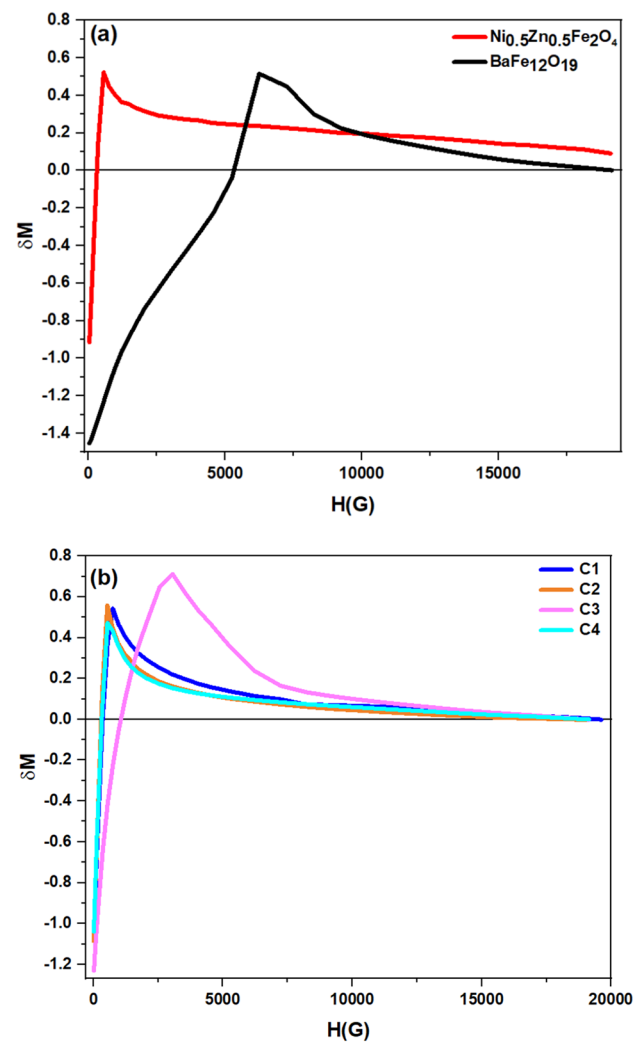

Fig. 8 Henkel plots of **a** pure BaFe$_{12}$O$_{19}$ and Ni$_{0.5}$Zn$_{0.5}$Fe$_2$O$_4$, **b** C1, C2, C3, and C4

where $m_d(H) = \frac{M_d(H)}{M_d(\infty)}$ is the demagnetization a $m_r(H) = \frac{M_r(H)}{M_r(\infty)}$ is the remanence magnetization, $M(\infty)$ is remanence in the saturated state. The exchange coupling interaction between the soft and hard phases of the nanocomposites is indicated by a positive value of δM, while dipolar interactions are indicated by a negative value of δM [64]. As shown in Figs. 8a,b, all pure ferrites and nanocomposites exhibit both positive and negative values of δM showing that both exchange and dipolar interactions are occurring. The positive δM part, however, is more important than the negative one. As a result, in all pure ferrites and nanocomposites, exchange coupling is the predominant kind of interaction. The magnitude and sign of δM can be used to
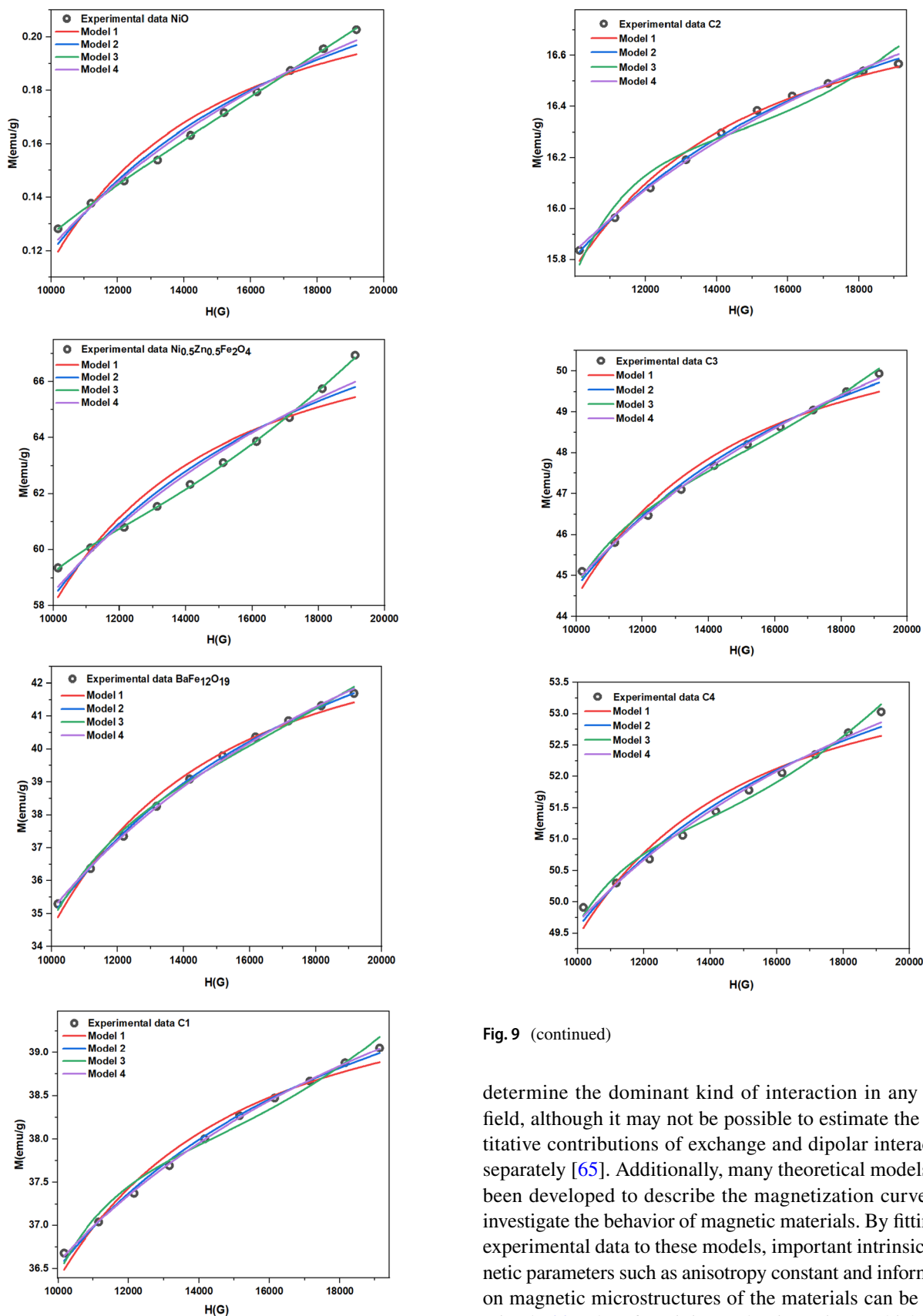
Fig. 9 LAS fitting for pure samples and nanocomposites

Fig. 9 (continued)

determine the dominant kind of interaction in any given field, although it may not be possible to estimate the quantitative contributions of exchange and dipolar interactions separately [65]. Additionally, many theoretical models have been developed to describe the magnetization curves and investigate the behavior of magnetic materials. By fitting the experimental data to these models, important intrinsic magnetic parameters such as anisotropy constant and information on magnetic microstructures of the materials can be determined [66]. Therefore, it is good to investigate which of the Laws of Approach to Saturation (LAS) better describes the

dependence of magnetization on the applied magnetic field. This is done by fitting the experimental magnetic data of the pure samples and nanocomposites with the Law of Approach to Saturation (LAS) [67]:

$$M(H) = M_s\left(1 - \frac{\alpha}{H} - \frac{\beta}{H^2}\right) + \gamma H \tag{6}$$

where M_s is the saturation magnetization, $\frac{\alpha}{H}$ is known as magnetic hardness and results from structural defects, $\frac{\beta}{H^2}$ is attributed to magnetocrystalline anisotropy with $\beta = \frac{8}{105} \times \frac{K^2}{\mu_0^2 M_s^2}$, μ_0 is the permeability of free space, K is the cubic anisotropy constant, and γH term is referred as a paramagnetism-like term. Equation (6) can be studied in different forms:

Model (1) assumes the H^{-2} dependency of the magnetization [68]:

$$M(H) = M_s\left(1 - \frac{\beta}{H^2}\right) \tag{7}$$

Model (2) merely comprises the term $\frac{\alpha}{H}$, which reflects the magnetization's deviation from saturation [69]:

$$M(H) = M_s\left(1 - \frac{\alpha}{H}\right) \tag{8}$$

Model (3) considers all the terms in Eq. (6).

Model (4) is given by the following equation [70]:

$$M(H) = M_s\left(1 - \left(\frac{H^*}{H}\right)^{\frac{1}{2}}\right) \tag{9}$$

H^* provides quantitative information on the non-saturation that corresponds to point defects and atomic-scale magnetic anisotropy variations. If the M-H loop is completely saturated, H^* will vanish. The fitting of the high applied field region (10 kG $< H <$ 20 kG) for the M-H data with the different LAS models is shown in Fig. 9 and the fitted parameters are listed in Table 5. One of the reliability parameters of a model is the goodness of fit (R^2), which is a constant value that should be approaching unity. The R^2 values for the used models are written in Table 5. Model (1) does not, in comparison to the other models, offer the best fit for the experimental data, as can be seen from the R^2 value. This could result from the significant impact of structural defects and linear magnetization factors, which cannot be ignored as suggested in Model 1. These structural defects may consist of dislocations, inhomogeneities, and grain boundaries [71]. The R^2 values indicate that model (2) provides a better fitting for the experimental data for all samples than model (1). The experimental data were not adequately described by model (3), which takes into consideration inhomogeneities

$\frac{\alpha}{H}$, anisotropy $\frac{\beta}{H^2}$, and differential susceptibility (γ) factors, as shown from the negative α and β values, despite the fits having acceptable reliability ($R^2 \sim 1$) for almost most of the samples. The negative values of (α) and (β) do not appear to have any meaningful physical significance. On the other hand, this result might be a sign that in our pure and composite samples, there is a dependence of magnetization on various forms of H rather than the summation of the $\frac{1}{H}$, $\frac{1}{H^2}$, and H in the field range (10 kG $< H <$ 20 kG) [68]. Model (4) offers a little better fitting for the experimental data for most pure and nanocomposite samples than model (2) according to R^2 values. The magnetization's deviation from the saturation term (α) in the model (2) and the non-saturation term (H^*) in the model (4) have almost a similar physical meaning, for this reason, we can find similar trends of variation of (α) and (H^*) for the different samples. Additionally, C2, the most saturated sample (Fig. 6II) has the lowest values of (α) and (H^*), and NiO, the least saturated sample (Fig. 6Ia) has the highest values of (α) and (H^*) as can be seen in Table 5. In conclusion, the data in the current study are best fitted to models (2) and (4) showing magnetization dependence on H^{-1} and $H^{-1/2}$, respectively, in the field range (10 kG $< H <$ 20 kG).

4 Conclusion

In summary, ternary NiO/BaFe$_{12}$O$_{19}$/Ni$_{0.5}$Zn$_{0.5}$Fe$_2$O$_4$ nanocomposites were prepared using the wet ball-milling process for different weight percentages of pure NiO, BaFe$_{12}$O$_{19}$, and Ni$_{0.5}$Zn$_{0.5}$Fe$_2$O$_4$ nanoparticles at a calcination temperature 950 °C. The three pure phases were synthesized by the co-precipitation method. The pure NiO and Ni$_{0.5}$Zn$_{0.5}$Fe$_2$O$_4$ were formed without impurities while α-Fe$_2$O$_3$ appeared as a secondary phase with BaFe$_{12}$O$_{19}$ as indicated by XRD results. The TEM microscopy revealed the cubic, quasi-spherical, and hexagonal morphologies of NiO, Ni$_{0.5}$Zn$_{0.5}$Fe$_2$O$_4$, and BaFe$_{12}$O$_{19}$, respectively, and the nanocomposites exhibited various morphologies corresponding to their constituent nanophases. The miller indices (hkl) obtained from XRD and SAED (hkl) were in agreement. Moreover, the high-resolution XPS measurements revealed the presence of the following oxidation states of the elements (Ba^{2+}, Ni^{2+}, Ni^{3+}, Zn^{2+}, Fe^{3+} and O^{2-}) in the pure samples and nanocomposites. The room temperature M-H loops, plotted from VSM data, showed a ferromagnetic behavior for all nanocomposites with different values of M$_s$, M$_r$, and H$_c$ that were affected by the weight percentage of each phase. One peak was observed in the SFD plots which indicated the exchange-coupled nanocomposites (C1, C2, and C4). Moreover, all pure and nanocomposites appear to follow the laws of approach to saturation (LAS) having a

Table 5 Extracted parameters from different LAS models for pure and nanocomposite samples

Models	Fitted parameters	NiO	$Ni_{0.5}Zn_{0.5}Fe_2O_4$	$BaFe_{12}O_{19}$	C1	C2	C3	C4
1	M_s (emu/g)	0.222	68.238	43.996	39.829	16.855	51.390	58.852
	$\beta \times 10^7$ (G^2)	4.815	1.496	2.149	0.866	0.647	1.349	0.820
	R^2	0.935	0.882	0.987	0.975	0.970	0.968	0.946
2	M_s (emu/g)	0.281	74.017	49.107	41.716	17.446	55.187	56.294
	α (KG)	5.771	2.120	2.890	1.249	0.939	1.898	1.191
	R^2	0.973	0.933	0.999	0.995	0.996	0.992	0.980
3	M_s (emu/g)	3.588E−4	0.041	0.501	0.278	−0.00265	−0.000379	0.51247
	α (KG)	−0.002	−0.015	−1.031E−3	−1.804E−3	8.527E−4	1.61E+06	−1.275E−3
	$\beta \times 10^7$ (G^2)	1.297E−3	6.460E−3	580.528	867.773	−41,289.400	−7.94E+05	589.244
	$\gamma \times 10^{-6}$ (emu g^{-1} G^{-1})	9.007	2110.000	1160.000	1000.000	408.931	1380.000	1400.000
	R^2	0.999	0.998	0.992	0.977	0.944	0.990	0.984
4	M_s (emu/g)	0.400	85.603	59.340	45.495	18.592	63.0808	61.607
	H^* (KG)	4.862	1.003	1.667	0.384	0.219	0.842	0.382
	R^2	0.986	0.954	0.998	0.999	0.989	0.998	0.993

magnetization dependency on H^{-1} and $H^{-1/2}$ separately, rather than the summation of H^{-1}, H^{-2}, and H, in the field range (10 kG $< H <$ 20 kG). The exchange-coupled nanocomposites can be useful in many magnetic and biomedical applications.

Declarations

Conflict of interest The authors declare that they have no conflict of interest.

References

1. S. Mourdikoudis, A. Kostopoulou, A.P. LaGrow, Adv. Sci. **8**, 2004951 (2021). https://doi.org/10.1002/advs.202004951
2. M.A. Almessiere, Y.A. Slimani, M. Hassan, M.A. Gondal, E. Cevik, A. Baykal, Int. J. Energy Res. **45**, 16691 (2021). https://doi.org/10.1002/er.6916
3. R. Pullar, Prog. Mater. Sci.. Mater. Sci. **57**, 1191 (2012). https://doi.org/10.1016/j.pmatsci.2012.04.001
4. C. Ross, Annu. Rev. Mater. Res.. Rev. Mater. Res. **31**, 203 (2001). https://doi.org/10.1146/annurev.matsci.31.1.203
5. Z. Durmus, A. Durmus, H. Kavas, J. Mater. Sci. **50**, 1201 (2015). https://doi.org/10.1007/s10853-014-8676-3
6. S.T. Abarna, R. EzhilVizhi, V. Harikrishnan, Results Phys. **48**, 106419 (2023). https://doi.org/10.1016/j.rinp.2023.106419
7. M. Naghdi, M. Ghovvati, N. Rabiee, S. Ahmadi, N. Abbariki, S. Sojdeh, A. Ojaghi, M. Bagherzadeh, O. Akhavan, E. Sharifi, M. Rabiee, M.R. Saeb, K. Bolouri, T.J. Webster, E.N. Zare, A. Zarrabi, Adv. Colloid Interface Sci. **308**, 102771 (2022). https://doi.org/10.1016/j.cis.2022.102771
8. E.F. Kneller, R. Hawig, IEEE Trans. Magn.Magn. **27**, 3588 (1991). https://doi.org/10.1109/20.102931
9. S. Torkian, A. Ghasemi, J. Magn. Magn. Mater.Magn. Magn. Mater. **469**, 119 (2019). https://doi.org/10.1016/j.jmmm.2018.07.018
10. N.A. Algarou, Y. Slimani, M.A. Almessiere, A. Baykal, New J. Chem. **44**, 5800 (2020). https://doi.org/10.1039/D0NJ00109K
11. K. Manglam, S. Kumari, J. Mallick, A. Shukla, M. Kar, Phys. Scr. **97**, 035809 (2022). https://doi.org/10.1088/1402-4896/ac53c5
12. M.A. Almessiere, Y. Slimani, H. Attia, S.I.M. Sheikh, A. Sadaqat, M.G. Vakhitov, D.S. Klygach, M. Sertkol, A. Baykal, A.V. Trukhanov, J. Market. Res. **15**, 1416 (2021). https://doi.org/10.1016/j.jmrt.2021.08.137
13. A. Bajorek, C. Berger, M. Dulski, P. Łopadczak, M. Zubko, K. Prusik, M. Wojtyniak, A. Chrobak, F. Grasset, N. Randrianantoandro, J. Phys. Chem. Solids **129**, 1 (2019). https://doi.org/10.1016/j.jpcs.2018.12.045
14. A.S. Fawzi, A.D. Sheikh, V.L. Mathe, J. Alloy. Compd. **502**, 231 (2010). https://doi.org/10.1016/j.jallcom.2010.04.152
15. A. Lohmaah, K. Chokprasombat, S. Pinitsoontorn, C. Sirisathitkul, Materials **14**, 5873 (2021). https://doi.org/10.3390/ma14195873
16. M. Yassine, N. El Ghouch, A.M. Abdallah, K. Habanjar, R. Awad, J. Alloy. Compd. **907**, 164501 (2022). https://doi.org/10.1016/j.jallcom.2022.164501
17. K.W. Moon, S.G. Cho, Y.H. Choa, K.H. Kim, J. Kim, Phys. Stat. Sol. (a) **204**, 4141 (2007). https://doi.org/10.1002/pssa.200777228
18. M. Yang, R. Jin, Z. Wang, J. Liu, R. Barua, X. Song, M. Zhang, J. Alloy. Compd. **820**, 153429 (2020). https://doi.org/10.1016/j.jallcom.2019.153429

19. S. Kumar, M. Kar, Ceram. Int. **48**, 30574 (2022). https://doi.org/10.1016/j.ceramint.2022.06.338

20. H. Nikmanesh, M. Moradi, P. Kameli, G.H. Bordbar, J. Electron. Mater. **46**, 5933 (2017). https://doi.org/10.1007/s11664-017-5576-8

21. M. Yang, J. Lu, X. Wang, H. Zhang, F. Chen, J. Sun, J. Yang, Y. Sun, G. Lu, Sens. Actuators B Chem. **313**, 127965 (2020). https://doi.org/10.1016/j.snb.2020.127965

22. F.I. Dar, K.R. Moonoosawmy, M. Es-Souni, Nanoscale Res. Lett. **8**, 363 (2013). https://doi.org/10.1186/1556-276X-8-363

23. X. Li, A. Dhanabalan, C. Wang, J. Power. Sources **196**, 9625 (2011). https://doi.org/10.1016/j.jpowsour.2011.06.097

24. F. Motahari, M.R. Mozdianfard, F. Soofivand, M. Salavati-Niasari, RSC Adv. **4**, 27654 (2014). https://doi.org/10.1039/c4ra02697g

25. D. Paul Joseph, M. Saravanan, B. Muthuraaman, P. Renugambal, S. Sambasivam, S. Philip Raja, P. Maruthamuthu, C. Venkateswaran, Nanotechnology **19**, 485707 (2008). https://doi.org/10.1088/0957-4484/19/48/485707

26. I. Hotovy, J. Huran, P. Siciliano, S. Capone, L. Spiess, V. Rehacek, Sens. Actuators B Chem. **103**, 300 (2004). https://doi.org/10.1016/j.snb.2004.04.109

27. M. Tyagi, M. Tomar, V. Gupta, AMR **488–489**, 103 (2012). https://doi.org/10.4028/www.scientific.net/AMR.488-489.103

28. W.J. Gong, W. Liu, D. Li, S. Guo, X.H. Liu, J.N. Feng, B. Li, X.G. Zhao, Z.D. Zhang, J. Appl. Phys. **109**, 07D711 (2011). https://doi.org/10.1063/1.3544505

29. R. Yassine, A.M. Abdallah, R. Awad, Z. Bitar, Physica B Condens. Matter **624**, 413444 (2022). https://doi.org/10.1016/j.physb.2021.413444

30. T. Munawar, F. Iqbal, S. Yasmeen, K. Mahmood, A. Hussain, Ceram. Int. **46**, 2421 (2020). https://doi.org/10.1016/j.ceramint.2019.09.236

31. J. Al Boukhari, A. Khalaf, R. Awad, Appl. Phys. A **126**, 74 (2020). https://doi.org/10.1007/s00339-019-3247-8

32. P. Xu, X. Han, M. Wang, J. Phys. Chem. C **111**, 5866 (2007). https://doi.org/10.1021/jp068955c

33. M. Radwan, M.M. Rashad, M.M. Hessien, J. Mater. Process. Technol. **181**, 106 (2007). https://doi.org/10.1016/j.jmatprotec.2006.03.015

34. S. Anjum, F. Sehar, Z. Mustafa, M.S. Awan, Appl. Phys. A **124**, 49 (2018). https://doi.org/10.1007/s00339-017-1456-6

35. C. Yu, A.S. Sokolov, P. Kulik, V.G. Harris, J. Alloy. Compd. **814**, 152301 (2020). https://doi.org/10.1016/j.jallcom.2019.152301

36. S. Hasan, B. Azhdar, Adv. Condens. Matter Phys. **2022**, 1 (2022). https://doi.org/10.1155/2022/4603855

37. B. Khongorzul, N. Jargalan, N. Tsogbadrakh, D. Odkhuu, S.V. Trukhanov, A.V. Trukhanov, D. Sangaa, Ceram. Int. **49**, 15492 (2023). https://doi.org/10.1016/j.ceramint.2023.01.134

38. L. Rifai, F. Fattouh, K. Habanjar, N. Yaacoub, R. Awad, J. Alloy. Compd. **868**, 159072 (2021). https://doi.org/10.1016/j.jallcom.2021.159072

39. O.-A. Lazar, A. Marinoiu, M. Raceanu, A. Pantazi, G. Mihai, M. Varlam, M. Enachescu, Energies **13**, 4307 (2020). https://doi.org/10.3390/en13174307

40. A. Aridi, R. Awad, A. Khalaf, Appl. Phys. A **127**, 206 (2021). https://doi.org/10.1007/s00339-021-04362-7

41. C. Pahwa, S.B. Narang, P. Sharma, J. Alloy. Compd. **815**, 152391 (2020). https://doi.org/10.1016/j.jallcom.2019.152391

42. A. Zielińska-Jurek, Z. Bielan, S. Dudziak, I. Wolak, Z. Sobczak, T. Klimczuk, G. Nowaczyk, J. Hupka, Catalysts **7**, 360 (2017). https://doi.org/10.3390/catal7120360

43. K. Habanjar, H. Shehabi, A.M. Abdallah, R. Awad, Appl. Phys. A **126**, 402 (2020). https://doi.org/10.1007/s00339-020-03497-3

44. O.M. Hemeda, N.Y. Mostafa, O.H. Abd Elkader, D.M. Hemeda, A. Tawfik, M. Mostafa, J. Magn. Magn. Mater.Magn. Magn. Mater. **394**, 96 (2015). https://doi.org/10.1016/j.jmmm.2015.05.059

45. A. Khalid, P. Ahmad, A.I. Alharthi, S. Muhammad, M.U. Khandaker, M.R.I. Faruque, A. Khan, I.U. Din, M.A. Alotaibi, K. Alzimami, A.A. Alfuraih, D.A. Bradley, Materials **14**, 3223 (2021). https://doi.org/10.3390/ma14123223

46. A.C. Gandhi, H.-H. Chiu, K.-T. Wu, C.-L. Cheng, S.Y. Wu, Appl. Surf. Sci. **536**, 147856 (2021). https://doi.org/10.1016/j.apsusc.2020.147856

47. S. Joshi, V.B. Kamble, M. Kumar, A.M. Umarji, G. Srivastava, J. Alloy. Compd. **654**, 460 (2016). https://doi.org/10.1016/j.jallcom.2015.09.119

48. R. Tholkappiyan, K. Vishista, Int. J. Mater. Res. **106**, 127 (2021). https://doi.org/10.3139/146.111161

49. W. Chehade, H. Basma, A.M. Abdallah, R. Sayed Hassan, R. Awad, Ceram. Int. **48**, 1238 (2022). https://doi.org/10.1016/j.ceramint.2021.09.209

50. L. Phor, S. Chahal, V. Kumar, J. Adv. Ceram. **9**, 576 (2020). https://doi.org/10.1007/s40145-020-0396-3

51. M. Suthar, A.K. Srivastava, R.K. Joshi, P.K. Roy, J. Mater. Sci. Mater. Electron. **31**, 16793 (2020). https://doi.org/10.1007/s10854-020-04234-5

52. J. Hu, F. Gao, Z. Zhao, S. Sang, P. Li, W. Zhang, X. Zhou, Y. Chen, Appl. Surf. Sci. **363**, 181 (2016). https://doi.org/10.1016/j.apsusc.2015.12.024

53. R. Kumar, S. Guha, R. Kr. Singh, M. Kar, J. Magn. Magn. Mater. Magn. Magn. Mater. **465**, 93 (2018). https://doi.org/10.1016/j.jmmm.2018.05.061

54. R. Yassine, A.M. Abdallah, R. Sayed Hassan, N. Yaacoub, R. Awad, Z. Bitar, Ceram. Int. **48**, 14825 (2022). https://doi.org/10.1016/j.ceramint.2022.02.019

55. T. Dippong, E. Andrea Levei, O. Cadar, I. GrigoreDeac, M. Lazar, G. Borodi, I. Petean, J. Alloys Compd. **849**, 156695 (2020). https://doi.org/10.1016/j.jallcom.2020.156695

56. R.K. Kotnala, S. Ahmad, A.S. Ahmed, J. Shah, A. Azam, J. Appl. Phys. **112**, 054323 (2012). https://doi.org/10.1063/1.4752030

57. D. Roy, C. Shivakumara, P.S. Anil Kumar, J. Magn. Magn. Mater. Magn. Magn. Mater. **321**, L11 (2009). https://doi.org/10.1016/j.jmmm.2008.09.017

58. K. Fukunaga, J. Kuma, Y. Kanai, IEEE Trans. Magn.Magn. **35**, 3235 (1999). https://doi.org/10.1109/20.800485

59. S.M. Suryawanshi, D.S. Badwaik, B.S. Shinde, K.D. Gaikwad, M. Shkir, K.V. Chandekar, S. Gundale, J. Mol. Struct.Struct. **1272**, 134173 (2023). https://doi.org/10.1016/j.molstruc.2022.134173

60. M.A. Almessiere, Y. Slimani, A. Baykal, Ceram. Int. **44**, 9000 (2018). https://doi.org/10.1016/j.ceramint.2018.02.101

61. A. Aridi, R. Awad, A. Khalaf, Phys. Scr. **96**, 105802 (2021). https://doi.org/10.1088/1402-4896/ac0e02

62. N.A. Algarou, Y. Slimani, M.A. Almessiere, F.S. Alahmari, M.G. Vakhitov, D.S. Klygach, S.V. Trukhanov, A.V. Trukhanov, A. Baykal, J. Market. Res. **9**, 5858 (2020). https://doi.org/10.1016/j.jmrt.2020.03.113

63. M.A. Almessiere, Y. Slimani, A.V. Trukhanov, A. Sadaqat, A.D. Korkmaz, N.A. Algarou, H. Aydın, A. Baykal, M.S. Toprak, Nano-Struct. Nano-Objects **26**, 100728 (2021). https://doi.org/10.1016/j.nanoso.2021.100728

64. R. Xiong, W. Li, C. Fei, Y. Liu, J. Shi, Ceram. Int. **42**, 11913 (2016). https://doi.org/10.1016/j.ceramint.2016.04.114

65. P. Karipoth, R.J. Joseyphus, J. Supercond. Nov. Magn.Supercond. Nov. Magn. **27**, 2123 (2014). https://doi.org/10.1007/s10948-014-2564-6

66. E.C. Devi, S.D. Singh, J. Supercond. Nov. Magn.Supercond. Nov. Magn. **34**, 15 (2021). https://doi.org/10.1007/s10948-020-05733-6

67. H. Zhang, D. Zeng, Z. Liu, J. Magn. Magn. Mater.Magn. Magn. Mater. **322**, 2375 (2010). https://doi.org/10.1016/j.jmmm.2010.02.040

68. E.C. Devi, I. Soibam, J. Supercond. Nov. Magn.Supercond. Nov. Magn. **32**, 1293 (2019). https://doi.org/10.1007/s10948-018-4823-4

69. S.L. Young, T.C. Wu, L. Horng, C.H. Lin, H.Z. Chen, M.C. Kao, C.R. Ou, N.F. Shih, J.B. Shi, J. Supercond. Nov. Magn. Supercond. Nov. Magn. **23**, 953 (2010). https://doi.org/10.1007/s10948-010-0651-x

70. M. Chithra, C.N. Anumol, B. Sahu, S.C. Sahoo, J. Magn. Magn. Mater.Magn. Magn. Mater. **424**, 174 (2017). https://doi.org/10.1016/j.jmmm.2016.10.064

71. A.M. Abdallah, R. Awad, Physica B Condens. Matter **629**, 413651 (2022). https://doi.org/10.1016/j.physb.2021.413651